Multiphysics simulation of tumor ablation in magnetic hyperthermia treatment

Jiang, Qian; Ren, Feng; Wang, Chenglei; Wang, Zhaokun; Kefayati, Gholamreza; Kenjeres, Sasa; Vafai, Kambiz; Cui, Xinguang; Liu, Yang; Tang, Hui

DOI
10.1016/j.ijheatmasstransfer.2025.126982

Publication date
2025

Document Version
Final published version

Published in
International Journal of Heat and Mass Transfer

Citation (APA)
Jiang, Q., Ren, F., Wang, C., Wang, Z., Kefayati, G., Kenjeres, S., Vafai, K., Cui, X., Liu, Y., & Tang, H. (2025). Multiphysics simulation of tumor ablation in magnetic hyperthermia treatment. *International Journal of Heat and Mass Transfer*, *245*, Article 126982. https://doi.org/10.1016/j.ijheatmasstransfer.2025.126982

International Journal of Heat and Mass Transfer 245 (2025) 126982

Contents lists available at ScienceDirect

International Journal of Heat and Mass Transfer

journal homepage: www.elsevier.com/locate/hmt

Multiphysics simulation of tumor ablation in magnetic hyperthermia treatment

Qian Jiang [a], Feng Ren [a,b], Chenglei Wang [a], Zhaokun Wang [a], Gholamreza Kefayati [c], Sasa Kenjeres [d], Kambiz Vafai [e], Xinguang Cui [f], Yang Liu [a], Hui Tang [a,*]

[a] Department of Mechanical Engineering, The Hong Kong Polytechnic University, Hong Kong, China
[b] School of Marine Science and Technology, Northwestern Polytechnical University, Xi'an, Shaanxi 710072, China
[c] School of Engineering, University of Tasmania, Hobart 7001, Tasmania, Australia
[d] Delft University of Technology, Faculty of Applied Sciences, Department of Chemical Engineering and J. M. Burgerscentrum Research School for Fluid Mechanics, Van der Maasweg 9, Delft 2629 HZ, The Netherlands
[e] Mechanical Engineering Department, University of California, Riverside, CA 92521, USA
[f] School of Aerospace Engineering, Huazhong University of Science and Technology, Wuhan, Hubei 430073, China

ARTICLE INFO

Keywords:
Magnetic hyperthermia
Interstitial tissue flow
Heat and mass transfer
Thermal dose

ABSTRACT

Magnetic hyperthermia is a promising cancer treatment method that involves complex multiphysics phenomena, including interstitial tissue fluid flow, magnetic nanoparticle (MNP) transport, and temperature evolution. However, these intricate processes have rarely been studied simultaneously, primarily due to the lack of a comprehensive simulation tool. To address this issue, we develop a comprehensive numerical framework in this study. Using this framework, we simulate a circular-shaped tumor embedded in healthy tissue. The treatment process is examined under two scenarios: one considering gravity and the other neglecting it. Without gravity, the interstitial tissue flow remains stationary, and hence MNP transport and temperature evolution are determined solely by diffusion. The optimal treatment time, when the tumor cells are completely ablated, decreases with both the Lewis number and the heat source number, following a power law. When gravity is considered, treatment efficacy deteriorates due to buoyancy-induced MNP movement, significantly extending the time required to completely ablate the tumor cells. This required time increases with both the buoyancy ratio and the Darcy ratio, also following a power law. The results from this study could provide valuable guidelines for practical magnetic hyperthermia treatment.

1. Introduction

Hyperthermia treatment or thermaltherapy is a cancer therapeutic treatment procedure emerging in recent decades in which tumor tissues are locally heated to approximately above 43 °C [1–6]. With the potential of only heating tumor cells to death while protecting the surrounding healthy tissue, hyperthermia can effectively avoid side effects encountered in conventional cancer treatment and therefore alleviate suffering. Among various hyperthermia modalities, magnetic hyperthermia is a promising one, in which magnetic nanoparticles (MNPs) are directly injected into the tumor tissue and generate controllable heat by applying a high-frequency alternating magnetic field (AMF) so that the target temperature can be achieved to ablate tumor cells [7,8]. Magnetite (Fe_3O_4) is a widely adopted MNP candidate due to its excellent magnetic properties and low toxicity [9–12]. The heat generated by MNPs is primarily associated with relaxation losses when exposed to the AMF, which can be predicted using the Rosensweig's model [13,14].

To guide the process before the actual treatment, a reliable modeling tool is required for fast predicting the treatment efficacy. Currently the most popular model is the Pennes bio-beat transfer equation (PBHTE), which was proposed by Pennes in 1948 based on laboratory observations of human muscle. It considers thermal energy balance, heat convection through blood perfusion and heat generation induced by MNPs. Due to its ease of implementation, PBHTE has been widely adopted in predictive studies of magnetic hyperthermia treatment [15–17]. However, it overlooks the interstitial tissue flow and actual mass transfer of MNPs. To enhance the prediction accuracy, therefore, researchers have been keen in incorporating other key factors into the model.

MNP concentration determines the distribution of heat source [18]. Some studies have incorporated the mass transfer of MNPs into the

---

* Corresponding author.
E-mail address: h.tang@polyu.edu.hk (H. Tang).

https://doi.org/10.1016/j.ijheatmasstransfer.2025.126982
Received 17 November 2024; Received in revised form 13 March 2025; Accepted 14 March 2025

Nomenclature

Abbreviations

AMF	Alternating magnetic field
CFD	Computational fluid dynamics
LBM	Lattice Boltzmann method
MNP	Magnetic nanoparticle
MRT	Multiple-relaxation-time
PBHTE	Pennes bio-beat transfer equation
REV	Representative elementary volume

Greek Letters

α	Thermal diffusivity, m^2/s
β_C	Solutal expansion coefficient, 1
β_T	Thermal expansion coefficient, 1/K
χ_0	Equilibrium susceptibility
μ_0	Magnetic permeability of the vacuum, Tm/A
ϕ	Porosity
ψ	Dimensionless concentration
ρ	Density, kg/m^3
σ	Thermal capacity ratio
σ_E	Electrical conductivity, S/m
τ_R	Effective relaxation time, s
θ	Dimensionless temperature
υ	Kinetic viscosity, m^2/s
t	Dimensionless time

Roman Letters

(X, Y)	Dimensionless Cartesian coordinate
(x, y)	Cartesian coordinate, m
$\dot{m}$	Mass flow rate of perfusing blood, kg/m^3-s
$\mathbf{F_M}$	Magntic Lorentz force, kg/m^2-s^2
$\mathbf{F}$	Total external body force, kg/m^2-s^2
$\mathbf{f}$	Particle distribution function for fluid field
$\mathbf{G}$	Gravity force, kg/m^2-s^2
$\mathbf{g}$	Particle distribution function for temperature field
$\mathbf{h}$	Particle distribution function for concentration field
$\mathbf{i}$	Unit vector in the x direction
$\mathbf{j}$	Unit vector in the y direction
$\mathbf{U}$	Dimensionless velocity
$\mathbf{u}$	Velocity, m/s
B_0	Magnetic induction amplitude, T
C	MNP concentration
c_p	Specific heat, J/(kg-K)
C_{EM}	Coefficient, a function of temperature
$CEM43$	Cumulative equivalent minutes at 43 °C, min
D	MNP mass diffusivity, m^2/s
d_p	Mean pore diameter of porous media, m
d_{tum}	Diameter of circular tumor, mm
Da	Darcy number
f	Frequency, Hz
F_ψ	Forchheimer coefficient of porous media
g	Acceleration of gravity, m/s^2
H	Magnetic field intensity, A/m
H_0	Magnetic field intensity amplitude, A/m
Ha	Hartmann number
K	Permeability of porous media, m^2
k	Thermal conductivity, m^2/s
L	Length of healthy tissue, mm
Le	Lewis number
N	Buoyancy ratio
P	Dimensionless pressure
p	Pressure, Pa
Pe	Peclet number
Pr	Prandtl number
Q	Heat release rate induced by MNPs, J/m^3-s
Q_s	Heat source number
r	Ratio for parameter variation
R_{CEM43}	Percentage ratio of area for $CEM43 \geq 60$ min
R_{Da}	Darcy ratio of tumor and healthy tissue
Ra	Rayleigh number
S	Area, m^2
T	Temperature, °C
t	Time, min

Subscripts

b	Blood
e	Effective value
f	Interstitial tissue fluid
h	Healthy tissue
h	Higher reference value
l	Lower reference value
max	Maximum value
n	Nanoparticles
nf	Nanofluid
opt	Optimal value
req	Required value
s	Porous solid
tum	Tumor tissue

PBHTE model, recognizing its crucial role in therapies [19,20]. The diffusion or convection–diffusion equations typically govern the temporal and spatial evolution of MNP concentration [21–23]. Soltani et al. [24] discussed the impact of MNP transfer, compared temperature profiles at various instants, and concluded that MNP diffusion reduces the maximum temperature while expanding the ablation region in a tumor. Moreover, as confirmed by Salloum et al. [25] in their experiment, the distribution of MNPs can be controlled through well planned injections especially when the injection flow rate is sufficiently low.

Interstitial tissue flow is a crucial factor during magnetic hyperthermia treatment. Researchers, such as Tang et al. [26,27], have investigated the interstitial flow field using the Brinkman equation, demonstrating that the velocity of interstitial tissue flow directly impacts the distribution of MNP concentration and, consequently, the temperature profile. Similar studies have also been conducted, where the Darcy equation is employed [28–31]. These investigations unveiled the significant influence of the interstitial flow on the treatment efficacy. The understanding of flow through porous media has been evolving beyond the conventional Darcy and Brinkman models, leading to several alternative approaches. Nithiarasu et al. [32] proposed a generalized non-Darcy model that considers both linear and non-linear resistant force components, convection, inertia, and external body forces [33,34]. This model can be mathematically incorporated into the Navier–Stokes equations [35], and has been shown to provide more reliable information about velocity [36]. Despite these advantages, this model has never been employed in the simulation of magnetic hyperthermia treatment.

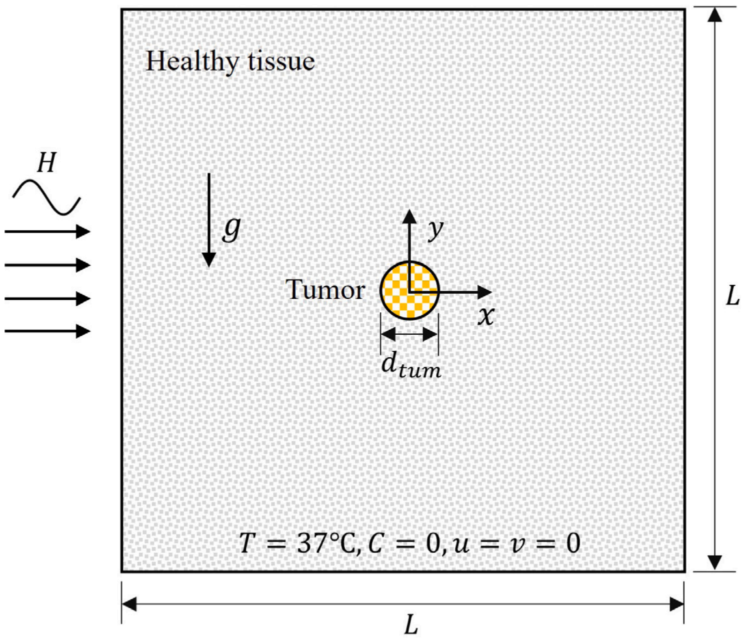

Fig. 1. Schematic of the two-dimensional magnetic hyperthermia problem in this study. The orange circular area denotes the tumor, whereas the outside gray region represents the healthy tissue. (For interpretation of the references to color in this figure legend, the reader is referred to the web version of this article.)

The density of MNPs is typically several times that of the tissue fluid [37,38]. Additionally, temperature difference also slightly influences the local flow density, which is commonly estimated as a buoyancy force using the Boussinesq approximation [39–42]. Consequently, the effect of gravity is significant in treatment [43–45]. The presence of gravity drives the interstitial tissue flow, thereby influencing the distribution of MNPs and temperature in the tumor tissue and healthy tissue, ultimately impacting the efficacy of treatment. However, this significant external force was often neglected in simulations of magnetic hyperthermia.

Ablation on tumor cells is a heat accumulation process, which is affected by both temperature level and duration of exposure. Dewhirst et al. [46] underscore the importance of these two factors, particularly in evaluating cell death where the temperature distribution is spatially and temporarily non-uniform. To quantify the thermal dose received by cells, a quantity termed cumulative-equivalent-minutes-at-43 °C ($CEM43$) is utilized. It accounts for both the temperature level and the duration of exposure, providing a standardized measure of thermal dose. Originally introduced by Sapareto and Dewey [47], $CEM43$ has been widely adopted in various studies to assess the efficacy of cell ablation during magnetic hyperthermia treatments [15,48,49].

In this study, we aim to develop a more accurate, holistic simulation framework for magnetic hyperthermia treatment, and use it to evaluate the treatment efficacy. This framework couples the Navier–Stokes equations for the interstitial tissue flow, a PBHTE variant for the heat generation, transfer and dissipation, and a concentration equation for the evolution of MNP distribution. The treatment efficacy is assessed using the $CEM43$ criterion. To demonstrate this framework, the treatment process on a simple tumor model, i.e., a tumor of circular shape surrounded by a block of healthy tissue, is simulated under various conditions. Results from two scenarios are presented and discussed, depending on whether gravity is considered. These findings have significant implications for practical magnetic hyperthermia treatment.

2. Methodology

2.1. Physical model

A schematic of the present two-dimensional magnetic hyperthermia problem is shown in Fig. 1, where a simple circular tumor is located at the center of a tissue block, subjected to an external high-frequency AMF of strength H. The diameter of the tumor is $d_{tum} = 10$ mm, which falls in the range of 90% observed tumor sizes [50]. The dimension of outside healthy tissue is chosen as $L = 10d_{tum}$, which is large enough for the study (as confirmed in Appendix A). To facilitate the following analysis and discussion, a Cartesian coordinate system is defined at the center of the tumor, with the x-axis pointing to the right and the y-axis pointing upward. We investigate the effect of gravity in this study, which is defined in the negative y direction.

Both tumor and healthy tissues are porous media with the same porosity $\phi = 0.26$ but different permeability K [51,52]. They are filled with the interstitial tissue fluid, which is assumed stationary before the treatment and remains incompressible and laminar throughout the process. Due to the small size of the tumor, the MNP is deemed to be injected into the tumor in one shot, uniformly occupying the entire tumor with a volume fraction of 0.01. Meanwhile, the initial temperature is set at 37 °C across the entire computational domain. The Boussinesq approximation is adopted due to the minor density variations in the interstitial flow. Additionally, we neglect the effects of Brownian diffusion and thermophoresis, as well as the influences of chemical reactions, metabolic heat, radiation, and viscous dissipation. We also assume local thermal equilibrium during the heat transfer process.

2.2. Governing equations

The multi-physics problem described above is studied numerically using a holistic simulation framework. Based on the mentioned assumptions, this framework is built upon the following set of equations [27, 35,40,53]

$$\nabla \cdot \mathbf{u} = 0, \tag{1a}$$

$$\frac{\partial \mathbf{u}}{\partial t} + (\mathbf{u} \cdot \nabla)\left(\frac{\mathbf{u}}{\phi}\right) = -\frac{1}{\rho_{nf}}\nabla(\phi p) + \upsilon_{nf}\nabla^2\mathbf{u} + \frac{\mathbf{F}}{\rho_{nf}}, \tag{1b}$$

$$\sigma\frac{\partial T}{\partial t} + \mathbf{u} \cdot \nabla T = \alpha_e\nabla^2 T + \frac{1}{(\rho c_p)_{nf}}\dot{m}_b c_{pb}(T_b - T) + C\frac{Q}{(\rho c_p)_{nf}}, \tag{1c}$$

$$\phi\frac{\partial C}{\partial t} + \mathbf{u} \cdot \nabla C = D_e\nabla^2 C, \tag{1d}$$

where $\nabla \equiv \frac{\partial}{\partial x}\mathbf{i}+\frac{\partial}{\partial y}\mathbf{j}$ is the gradient operator. **i** and **j** are the unit vectors in the x and y directions, respectively.

Eq. (1) includes the continuity equation, the momentum equation, the energy equation (a variant of PBHTE), and the concentration equation, respectively, applied in two-dimensional space to both tumor and healthy tissues. $\mathbf{u}$ is the flow velocity vector, with components u and v along x-axis and y-axis, respectively. T and C are the temperature and MNP concentration (i.e., volume fraction), respectively. p, ρ, c_p and v are fluid pressure, density, specific heat, and kinetic viscosity, respectively. $\sigma = [(\rho c_p)_{nf}\phi + (\rho c_p)_s(1-\phi)]/(\rho c_p)_{nf}$ is the heat capacity ratio. $\alpha_e = k_e/(\rho c_p)_{nf}$ is the effective thermal diffusivity, where $k_e = k_{nf}\phi + k_s(1-\phi)$ [54,55] represents the effective thermal conductivity of porous media. Here, the subscript "e" denotes the effective properties, "nf" denotes the properties of nanofluid, which is a mixture of the interstitial tissue fluid and the injected MNPs, and "s" denotes the property of porous solid. In addition, the subscript "b" in Eq. (1c) denotes the properties of perfusing blood. Note that the thermal properties are identical for interstitial tissue fluid, perfusing blood, and the porous solid in both tumor and healthy tissue, due to the minor differences among them [27,36,37,51]. The effective concentration diffusivity of MNPs in porous media is given by $D_e = \phi D$ [55], where D represents the concentration diffusivity in the pure fluid.

$\mathbf{F}$ in the last term of Eq. (1b) represents the total external body force, including the resistance forces from porous media, the buoyancy force induced by temperature and concentration gradients, and the Lorentz force induced by the AMF [40]

$$\mathbf{F} = -\frac{\phi\rho_{nf}v_{nf}}{K}\mathbf{u} - \frac{\phi\rho_{nf}F_\phi}{\sqrt{K}}|\mathbf{u}|\mathbf{u} + \phi\mathbf{G} + \phi\mathbf{F_M}. \tag{2}$$

The two resistance forces in porous media (the first two terms on the right-hand side, known as the Darcy and Forchheimer terms, respectively) are evaluated using the representative elementary volume (REV) scale method [40,56]. Here, $F_\phi = 1.75/\sqrt{150\phi^3}$ denotes the Forchheimer coefficient of porous media, $K = (\phi^3 d_p^2)/[150(1-\phi)^2]$ denotes the permeability, and d_p is mean pore diameter. Since the tumor and healthy tissues have different permeability, we use K_{tum} and K_h to denote their respective permeability.

The buoyancy force $\mathbf{G}$ is given by [57]

$$\mathbf{G} = g[(\rho\beta_T)_{nf}(T - T_l) + (\rho\beta_C)_{nf}(C - C_l)]\mathbf{j}, \tag{3}$$

where g is the gravitational acceleration. $(\rho\beta_T)_{nf}$ and $(\rho\beta_C)_{nf}$ represent the nanofluid's thermal expansion coefficient and concentration expansion coefficient, respectively. T_l and C_l represent the lower reference temperature and concentration, respectively.

$\mathbf{F_M}$ is the unsteady Lorentz force induced by a high-frequency AMF applied along the x direction, which, for simplicity, can be represented by an equivalent steady force as (see Appendix B for the detailed derivation and verification)

$$\mathbf{F_M} = -\frac{1}{2}\sigma_{Enf}B_0^2 v\mathbf{j}, \tag{4}$$

where σ_{Enf} is the electrical conductivity of nanofluid. B_0 is the amplitude of magnetic induction, which is proportional to the amplitude of the magnetic field intensity H_0, i.e., $B_0 = \mu_0 H_0$, where μ_0 is the magnetic permeability in vacuum.

Eq. (1c) is a variant of PBHTE, which includes the heat sink caused by blood perfusion $\dot{m}_b c_{pb}(T_b - T)$ and the heat source induced by the MNP exposed to AMF, CQ. $T_b = 37$ °C is the temperature of the perfusing blood and $\dot{m}_b$ is its mass flow rate. According to the experimental data of Lang et al. [58], $\dot{m}_b$ is a temperature-dependent variable and can be evaluated as

In healthy tissue:

$$\dot{m}_b = \begin{cases} 0.45 + 3.55\exp[-(T - 45.0)^2/12.0], & T \le 45.0\ °\text{C} \\ 4.0, & T > 45.0\ °\text{C}. \end{cases} \tag{5}$$

Table 1

Properties of nanofluid.

Tissue fluid properties	Value	MNP properties	Value
ρ_f (kg/m^3)	1052 [37]	ρ_n (kg/m^3)	5200 [38]
k_f (W/m K)	0.5 [37]	k_n (W/m K)	6 [38]
c_{pf} (J/kg K)	3800 [37]	c_{pn} (J/kg K)	670 [38]
β_{Tf} (1/K)	2.1×10^{-4} [38]	β_{Tn} (1/K)	1.3×10^{-5} [38]
σ_{Ef} (Ω^{-1} m^{-1})	0.7 [60]	σ_{En} (Ω^{-1} m^{-1})	2.5×10^4 [38]
μ_f (Pa s)	6.92×10^{-4} [61]	–	–

In tumor:

$$\dot{m}_b = \begin{cases} 0.833, & T < 37.0\ °\text{C} \\ 0.8333 - (T - 37.0)^{4.8}/5438.0, & 37.0 < T \le 42.0\ °\text{C} \\ 0.416, & T > 42.0\ °\text{C}. \end{cases} \tag{6}$$

The heat release rate Q is evaluated as the MNP power dissipation and can be calculated using Rosensweig's model [14]

$$Q = \pi\mu_0\chi_0 H_0^2 f\frac{2\pi f\tau_R}{1 + (2\pi f\tau_R)^2}. \tag{7}$$

where f is the frequency of the AMF and χ_0 is the equilibrium susceptibility. τ_R denotes the effective relaxation time, which is determined by both the Neel and Brownian relaxation time [11].

The effective properties of tissue fluid can be obtained by considering the MNP distribution, as [38,59]

$$\rho_{nf} = C\rho_n + (1 - C)\rho_f, \tag{8a}$$

$$v_{nf} = \frac{\mu_f}{\rho_{nf}(1 - C)^{2.5}}, \tag{8b}$$

$$(\rho c_p)_{nf} = C(\rho c_p)_n + (1 - C)(\rho c_p)_f, \tag{8c}$$

$$(\rho\beta_T)_{nf} = C(\rho\beta_T)_n + (1 - C)(\rho\beta_T)_f, \tag{8d}$$

$$k_{nf} = k_f\frac{k_n + 2k_f - 2C(k_f - k_n)}{k_n + 2k_f + C(k_f - k_n)}, \tag{8e}$$

$$\sigma_{Enf} = \sigma_{Ef}\frac{\sigma_{Ef} + 2\sigma_{Ef} - 2C(\sigma_{Ef} - \sigma_{Ef})}{\sigma_{Ef} + 2\sigma_{Ef} + C(\sigma_{Ef} - \sigma_{Ef})}, \tag{8f}$$

where the subscript "f" denotes pure fluid and "n" denotes Fe_3O_4 nanoparticles. Their proprieties are listed in Table 1.

If we choose d_{tum}, α_f, ρ_f, $T_h - T_l$ and $C_h - C_l$ as the repeating variables ($T_h = 47$ °C, $T_l = 37$ °C, $C_h = 0.01$, $C_l = 0.$), Eq. (1) can be nondimensionalized as

$$\nabla^* \cdot \mathbf{U} = 0, \tag{9a}$$

$$\begin{aligned} &\frac{\partial\mathbf{U}}{\partial\tau} + (\mathbf{U}\cdot\nabla^*)\left(\frac{\mathbf{U}}{\phi}\right) \\ &= -\frac{\rho_f}{\rho_{nf}}\nabla^*(\phi P) + Pr\frac{v_{nf}}{v_f}\nabla^{*2}\mathbf{U} - \phi\frac{v_{nf}}{v_f}\frac{Pr}{Da}\mathbf{U} - \phi\frac{F_\phi}{\sqrt{Da}}\sqrt{|\mathbf{U}|}\mathbf{U} \\ &+ \left\{\phi\frac{\rho_f}{\rho_{nf}}RaPr\left[\frac{(\rho\beta_T)_{nf}}{(\rho\beta_T)_f}\theta + \frac{(\rho\beta_C)_{nf}}{(\rho\beta_C)_f}N\varphi\right] - \phi\frac{\sigma_{Enf}}{\sigma_{En}}\frac{\rho_f}{\rho_{nf}}Ha^2 Pr\mathbf{U}\right\}\mathbf{j}, \end{aligned} \tag{9b}$$

$$\sigma\frac{\partial\theta}{\partial\tau} + \mathbf{U}\cdot\nabla^*\theta = \frac{\alpha_e}{\alpha_f}\nabla^{*2}\theta - \frac{(\rho c_p)_f}{(\rho c_p)_{nf}}Pe\theta + \varphi\frac{(\rho c_p)_f}{(\rho c_p)_{nf}}Q_s, \tag{9c}$$

$$\phi\frac{\partial\varphi}{\partial\tau} + \mathbf{U}\cdot\nabla^*\varphi = \frac{\phi}{Le}\nabla^{*2}\varphi, \tag{9d}$$

where the original dimensional parameters appear in either Capital letters or Greek letters as

$$\begin{aligned} &X = \frac{x}{d_{tum}},\ Y = \frac{y}{d_{tum}},\ \mathbf{U} = \frac{\mathbf{u}d_{tum}}{\alpha_f},\ \tau = \frac{t\alpha_f}{d_{tum}^2}, \\ &P = \frac{pd_{tum}^2}{\rho_f\alpha_f^2},\ \theta = \frac{T - T_l}{T_h - T_l},\ \varphi = \frac{C - C_l}{C_h - C_l}, \end{aligned} \tag{10}$$

and $\nabla^* \equiv \frac{\partial}{\partial X}\mathbf{i} + \frac{\partial}{\partial Y}\mathbf{j}$. From Eq. (9), this present problem is characterized by the following eight key dimensionless parameters:

$$Pr = \frac{\upsilon_f}{\alpha_f}, \tag{11a}$$

$$Da = \frac{K}{d_{tum}^2}, \tag{11b}$$

$$Ra = \frac{\beta_{Tf} g (T_h - T_l) d_{tum}^3}{\upsilon_f \alpha_f}, \tag{11c}$$

$$N = \frac{\beta_C (C_h - C_l)}{\beta_{Tf} (T_h - T_l)}, \tag{11d}$$

$$Ha = \mu_0 H_0 d_{tum} \sqrt{\frac{\sigma_{En}}{\rho_f \upsilon_f}}, \tag{11e}$$

$$Pe = \frac{\dot{m}_b c_{pb} d_{tum}^2}{(\rho c_p)_f \alpha_f}, \tag{11f}$$

$$Q_s = \frac{Q L^2 (C_h - C_l)}{(\rho c_p)_f \alpha_f (T_h - T_l)}, \tag{11g}$$

$$Le = \frac{\alpha_f}{D}. \tag{11h}$$

Pr, Da, Ra, N, Ha, Pe, Q_s and Le are the Prandtl number, Darcy number, Rayleigh number, buoyancy ratio, Hartmann number, Peclet number, heat source number and Lewis number, respectively. Pr is the ratio of momentum diffusivity to thermal diffusivity. Da reflects the effect of the permeability of the porous media. Ra quantifies the stability and behavior of fluid flow in the presence of buoyancy-driven convection. N is the ratio of the MNP buoyancy force to the thermal buoyancy force. Ha characterizes the influence of a magnetic field on the flow of a conducting fluid. Pe presents the importance of the convective and diffusive transport process in a fluid flow. Q_s specifies the heating ability of the MNP. Le denotes the ratio of thermal diffusivity and MNP mass diffusivity.

Since some properties differ between the tumor and the healthy tissue – such as the permeability K and the blood mass flow rate $\dot{m}_b$ – Da and Pe have different values in these two tissues. To address the influence of the difference in Da, we define a ratio of the Darcy numbers, as

$$R_{Da} = \frac{Da_{tum}}{Da_h} = \frac{K_{tum}}{K_h}. \tag{12}$$

Note that, Pe is linked to $\dot{m}_b$, a temperature-dependent variable (see Eqs. (5) and (6)). This means that Pe is temporarily varying and spatially non-uniform during the treatment.

Eq. (1) is solved using the multiple-relaxation-time Lattice Boltzmann method (MRT-LBM), with the D2Q9 (i.e., two-dimensional nine-discrete velocity) scheme applied on the fluid field and the D2Q5 (i.e., two-dimensional five-discrete velocity) scheme applied on the temperature and concentration fields [40]. More details about the numerical method of the LBM scheme and the adopted boundary conditions can be found in Appendix A.

2.3. Thermal dose

To evaluate the treatment efficacy, we adopt the widely accepted cumulative-equivalent-minutes-at −43 °C ($CEM43$) model to evaluate the thermal dose, as

$$CEM43 = \sum_{i=1}^{l} C_{EM}{}^{43-T_i} \delta t, \tag{13}$$

where T_i is the averaged temperature in °C at the ith time step, δt is the time interval, and l denotes the total number of time steps. The coefficient C_{EM} is 0.5 when $T_i > 43$ °C and 0.25 otherwise [47]. As $CEM43$ reaches 60 min, cells are regarded as completely ablated [15,46]. The higher the treatment temperature, the shorter the treatment time [62].

Table 2
Dimensionless parameters in baseline case [27,37,51,52].

Parameters	Value
Pr	5.26
Da_h	2.00×10^{-9}
Ra	2.50×10^{5}
N	−18.78
Ha	0.43
Q_s	5.73
Le	125
R_{Da}	4.84

With $CEM43$, we can further assess the therapeutic efficacy using an ablated area ratio for the tumor or surrounding healthy tissue, i.e.

$$R_{CEM43} = \frac{S_{CEM43 \geq 60 \ \text{min}}}{S_{tum}}. \tag{14}$$

Apparently, the optimal R_{CEM43} is 1 in the tumor and 0 in healthy tissue, respectively, in accordance with the expected hyperthermia treatment efficacy – killing all the tumor cells while leaving the healthy tissue unharmed.

Compared with the method adopted in our previous work [63], where the treatment efficacy is evaluated based on the time-frozen MNP distribution-determined temperature field, the current $CEM43$ model is more realistic, addressing the evolution of the MNP distribution and temperature during the treatment.

3. Results and discussion

In this study, we consider two scenarios: in one scenario the gravity is not considered, denoted as the “no-gravity” case, and in the other scenario the gravity along negative y direction is considered, denoted as the “with-gravity” case. According to Eqs. (1) and (2), the existence of gravity can induce the buoyancy force as a consequence of spatial difference in temperature or MNP concentration, which then drives the interstitial fluid flow. This induced flow may in return influence the MNP concentration and temperature distribution, and hence influence the treatment efficacy.

In each scenario a baseline case is chosen to facilitate analysis and comparison. The properties of the baseline cases are listed in Table 2, which are in the non-dimensional form and derived from typical values obtained from medical cases.

In this study, we mainly focus on the effects of four important parameters, namely Le, Q_s, N, and R_{Da}. The considerations are as follows. Le is a parameter related to MNP diffusion and hence influences the distribution of the MNP during the treatment [64]. Q_s reflects the heat generation capability of MNPs when exposed to AMF, affected by MNP effective relaxation time, the AMF amplitude and frequency [14,17,65]. These two parameters are closely related to the injected MNP and heat source distribution. N compares the temperature inhomogeneity-induced buoyancy force and the MNP concentration-induced buoyancy force. The negative sign indicates the opposite directions of these two buoyancy forces. R_{Da} describes the permeability difference between tumor and healthy tissues, which affects the porosity-related resistance according to Eq. (9b). As such, these two parameters are closely related to gravity and are hence important when buoyancy is involved.

For the convenience of comparison, four corresponding ratios of the value in studied cases to that in the baseline case, i.e., r_{Le}, r_{Qs}, r_N, and r_{RDa}, are used to describe the variation of these four parameters.

3.1. No-gravity scenario

When there is no gravity, no interstitial tissue flow will be induced according to Eq. (1). As such, only thermal and solutal diffusion is involved in the system dynamics. Fig. 2 presents the evolution of

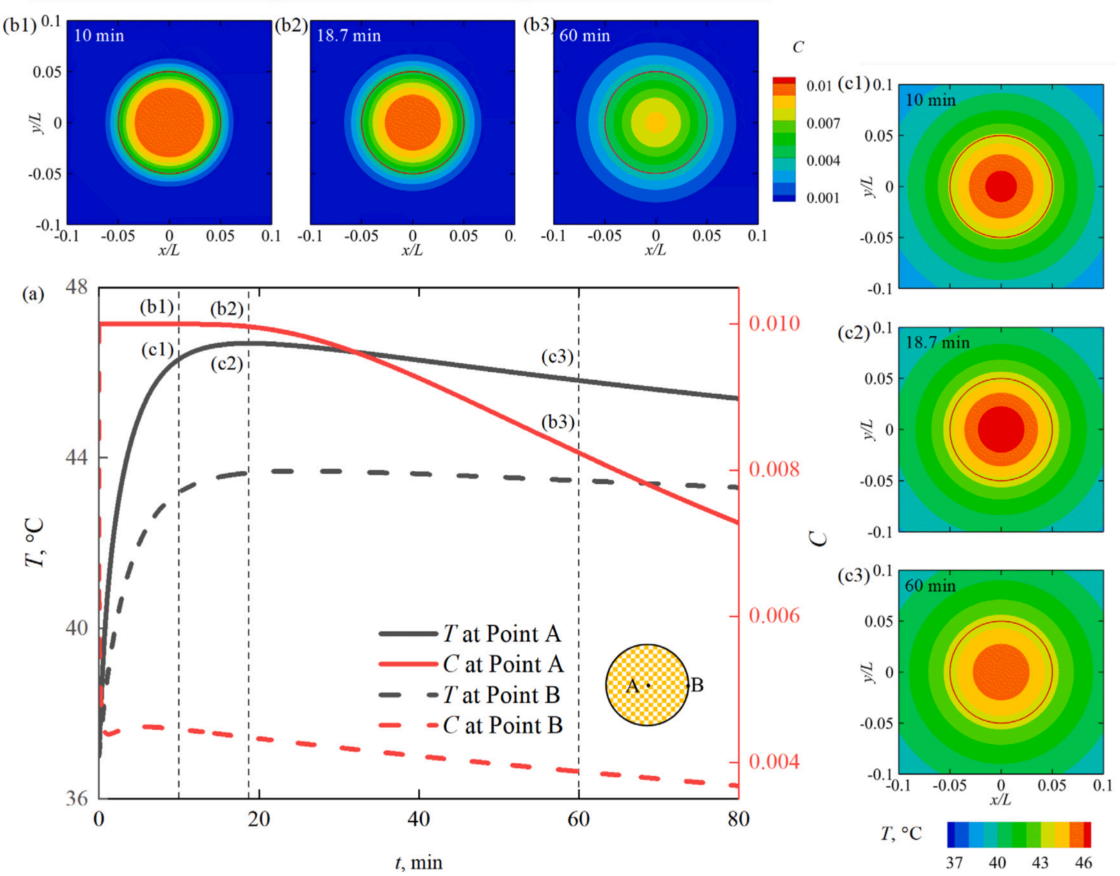

Fig. 2. (a) Evolution of MNP and temperature at the tumor center (point A, by solid lines) and tumor boundary (point B, by dashed lines), with distribution at some specific instants for baseline case. (b1)~(b3) denote MNP concentration distribution at $t = 10$ min, $t = 18.7$ min, and $t = 60$ min, respectively; (c1)~(c3) denote the temperature distribution at $t = 10$ min, $t = 18.7$ min, and $t = 60$ min, respectively.

MNP concentration and temperature at the tumor center (point A) and boundary (point B), as well as their contours at $t = 10$, 18.7 and 60 min for the baseline case. As shown in Fig. 2(a), at point A, the MNP concentration maintains its initial value ($C = 0.01$) for about 10 min, and then significantly decreases due to mass diffusion. As the result, its temperature rises very rapidly from 37 °C in the first 10 min, reaches the peak of 46.7 °C at about $t = 18.7$ min, and then gradually decreases. On the contrary, at point B, the MNP concentration rapidly drops to about 0.0044 within 1.2 min due to the largest concentration gradient across the boundary, which is then followed by a much mild decrease. Consequently, the temperature only rises to its peak 43.7 °C in the first 25.6 min, then almost maintains this value for quite a long time. When the treatment time is long enough, e.g., at $t = 60$ min, the MNP concentration at point B is only 47.1% of that at point A, whereas its temperature is 2.4 °C lower.

Since there is no induced flow, all the concentration and temperature contours appear in circles, which are centered at the tumor center, and evolve uniformly in all radial directions, as revealed in Fig. 2(b) and (c). $Le = 125$ for this case means that the thermal diffusion is about two orders of magnitudes faster than the solutal diffusion. This is clearly evidenced by the contours. For example, if we define 10% of the initial value as the boundary of the C contour (i.e., the $C = 0.001$ line) and the 10% temperature increase in the range of 37 °C to 47 °C as the boundary of the T contour (i.e., the $T = 38$ °C line), the diameter of the C contour is only 40.0% that of the T contour at 10 min.

Fig. 3(a) illustrates the time history of R_{CEM43} in the tumor and healthy tissues. It is found that $R_{CEM43} = 0$ in both tissues before $t = 11.7$ min (dash line (b)), where no ablation occurs. At $t = 11.7$ min, $CEM43 = 60.0$ min right at the tumor center, as revealed in Fig. 3(b), indicating that the ablation starts from this place. After that, the ablation region gradually expands until $t = 46.6$ min (dash line (c)), when the entire tumor is destroyed meanwhile the healthy tissue is unharmed (see Fig. 3(c)). The 34.9 min difference between the start and end of the ablation is due to the spatial temperature difference in the tumor, which is 3.1 °C (46.5 °C at the tumor center and 43.4 °C at the tumor boundary) at $t = 11.7$ min. In this baseline case, the treatment shall be terminated at $t = 46.6$ min, where $R_{CEM43} = 1$ for the tumor and $R_{CEM43} = 0$ for the healthy tissue, otherwise the healthy tissue will be ablated, as revealed in Fig. 3(a). As such, this instant is defined as the optimal treatment time t_{opt}.

Fig. 4(a) presents the variations of the optimal treatment time t_{opt} against the Lewis number Le and the heat source number Q_s, while the other parameters are kept the same as in the baseline case. It is seen that in general t_{opt} reduces with Le and Q_s, but is more sensitive to Q_s than Le. Specifically, the variation of t_{opt} against r_{Le} for a given constant $r_{Q_s} = 1.0$ is presented in Fig. 4(b). It appears that t_{opt} follows a power law with r_{Le} (data fitting with $R^2 = 0.998$ gives $t_{opt} = 2586Le^{-1.24} + 40.0$ min). As Le approaches 0, t_{opt} approaches infinity since the MNP diffuses immediately and cannot generate meaningful heat for the treatment. In this extreme case, the temperatures at both the tumor center (point A) and the tumor boundary (point B) remain at 37 °C, as depicted by the bottom horizontal line in Fig. 4(d). Even though when Le is non-zero but a small value, the treatment is very inefficient. For example, at $r_{Le} = 0.2$, 14% of tumor cells still survive after a treatment lasting for 150 min.

As Le approaches infinity, t_{opt} approaches 40.0 min since the MNP is “frozen” and its generated heat can completely kill all the tumor cells within 40.0 min. In this case, the temperature at the tumor center will reach within 0.1 °C of its final asymptotic value (47.5 °C) in 28.5 min, and the temperature at the tumor boundary will reach within 0.1 °C

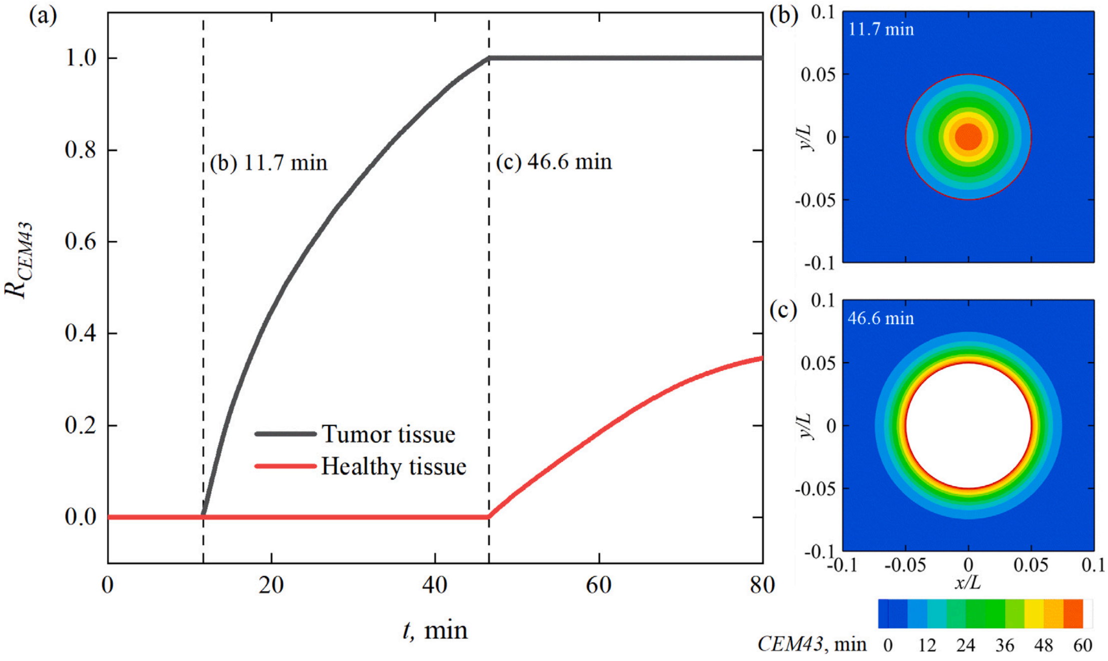

Fig. 3. (a) Evolution of R_{CEM43} in the tumor and healthy tissue for baseline case. (b) and (c) denote the distribution of $CEM43$ at $t = 11.7$ min and 46.6 min, respectively. The white region denotes the ablation part.

of its final asymptotic value (44.1 °C) in 28.2 min, both forming the upper bound of their respective groups as depicted in Fig. 4(d). Note that, the 40.0 min appearing here and the power law is obtained under the condition that all the other parameters are fixed at the baseline values, and it may change with the chosen baseline values.

The variation of t_{opt} against r_{Qs} for a given constant $r_{Le} = 1.0$ is presented in Fig. 4(c). Similar to the trend of varying Le, t_{opt} also follows a power law with r_{Qs} (data fitting with $R^2 = 0.976$ gives $t_{opt} = 40544 Q_s^{-3.84}$ min). It is obvious that as Q_s approaches 0, t_{opt} approaches infinity since no heat will generated for the treatment. In this case, the temperatures in the entire tumor remain at 37 °C, as depicted as the bottom horizontal line in Fig. 4(e). As Q_s approaches infinity, on the other hand, t_{opt} approaches 0 since the infinite heat can immediately enhance the temperature of the tumor to a very high level. In this case, the tumor cells can be completely killed in almost no time according to the $CEM43$ criterion. However, in practice Q_s cannot be too large, since the product of frequency and amplitude of magnetic field should not exceed 5×10^9 A/m-s in order to ensure the comfort of patients during the treatment [66]. Note that, the corresponding value for fH_0 equals 1.28×10^9 A/m s at $Q_s = 5.73$ in the baseline case [7]. As illustrated in Eqs. (7) and (11g), $(Q_s)_{max}$ can be 85.1 when increasing H_0 with unchanged f, 15.2 times the baseline Q_s value, which leads to the optimal treatment time of only $t_{opt} = 0.6$ min.

To account for the combined influence of both Le and Q_s, a two-dimensional fitting function is obtained. The optimal treatment time t_{opt} follows a power law relationship with the variation of both r_{Le} and r_{Qs}. The data fitting results in $R^2 = 0.946$, yielding an equation $t_{opt} = (4097386 Le^{-1.35} + 20714) Q_s^{-3.58}$ min. It indicates that as both Le and Q_s approach 0, the optimal treatment time t_{opt} tends towards infinity. Conversely, as Le and Q_s both increase towards infinity, t_{opt} approaches 0. This behavior is consistent with the practical treatment expectations.

From Fig. 4(d) and (e), one can see that a temperature peak (T_{max}) appears during each treatment. Since an extremely high temperature treatment may cause serious inflammation [67], T_{max} shall be monitored during the treatment. The T_{max} values at the tumor center, which represent the peak temperature over the entire tumor, and their occurrence time are listed in Table 3. As already mentioned at the beginning of this section, in the baseline case ($r_{Le} = r_{Qs} = 1$), $T_{max} = 46.7$ °C and it occurs at $t = 18.7$ min. As r_{Le} increases, T_{max} increases but occurs later. This is not surprising because fast diffusion (low Le) leads to a fast drop in the MNP concentration in the tumor, resulting in an early but low temperature peak. On the contrary, although T_{max} also increases with r_{Qs}, its occurrence time reduces, which is straightforward since large heat generation (high Q_s) leads to a fast and high temperature peak. It is also observed that T_{max} depends more on Q_s: doubling r_{Qs} to 2.0 leads to a much higher T_{max} of 54.5 °C.

Table 3
Temperature peak T_{max} and occurrence time t at tumor center (Point A).

r_{Le}	T_{max}, °C	t, min	r_{Qs}	T_{max}, °C	t, min
0.2	45.3	11.0	0.7	45.1	21.4
0.6	46.4	15.7	0.8	45.9	19.9
1.0	46.7	18.7	1.0	46.7	18.7
2.0	47.0	23.2	1.2	48.3	16.9
4.0	47.2	29.3	1.4	49.8	15.9
8.0	47.3	36.1	1.6	51.4	15.3
16.0	47.4	43.5	2.0	54.5	14.6

3.2. With-gravity scenario

When the gravity is introduced along the negative y direction, a buoyancy flow will be induced due to the MNP concentration difference (as the ideal MNP material magnetite is substantially heavier than interstitial tissue fluid [10,11]) and temperature difference. In the selected baseline case the buoyancy ratio is $N = -18.78$, which means the solutal buoyancy force is opposite in direction to the thermal buoyancy force, and the former outweighs the latter [57,68,69]. As such, the interstitial tissue fluid will be driven downward according to Eq. (1). This buoyancy flow can affect the treatment efficacy and is hence discussed in this section.

Fig. 5 presents the evolution of MNP concentration and temperature at four selected locations: the tumor center - point A, the rightmost point of the tumor - point B, its top point - point C, and its bottom point - point D, as well as the concentration and temperature contours at two selected instants: $t = 18.1$ and 60 min. It is evident from the contours

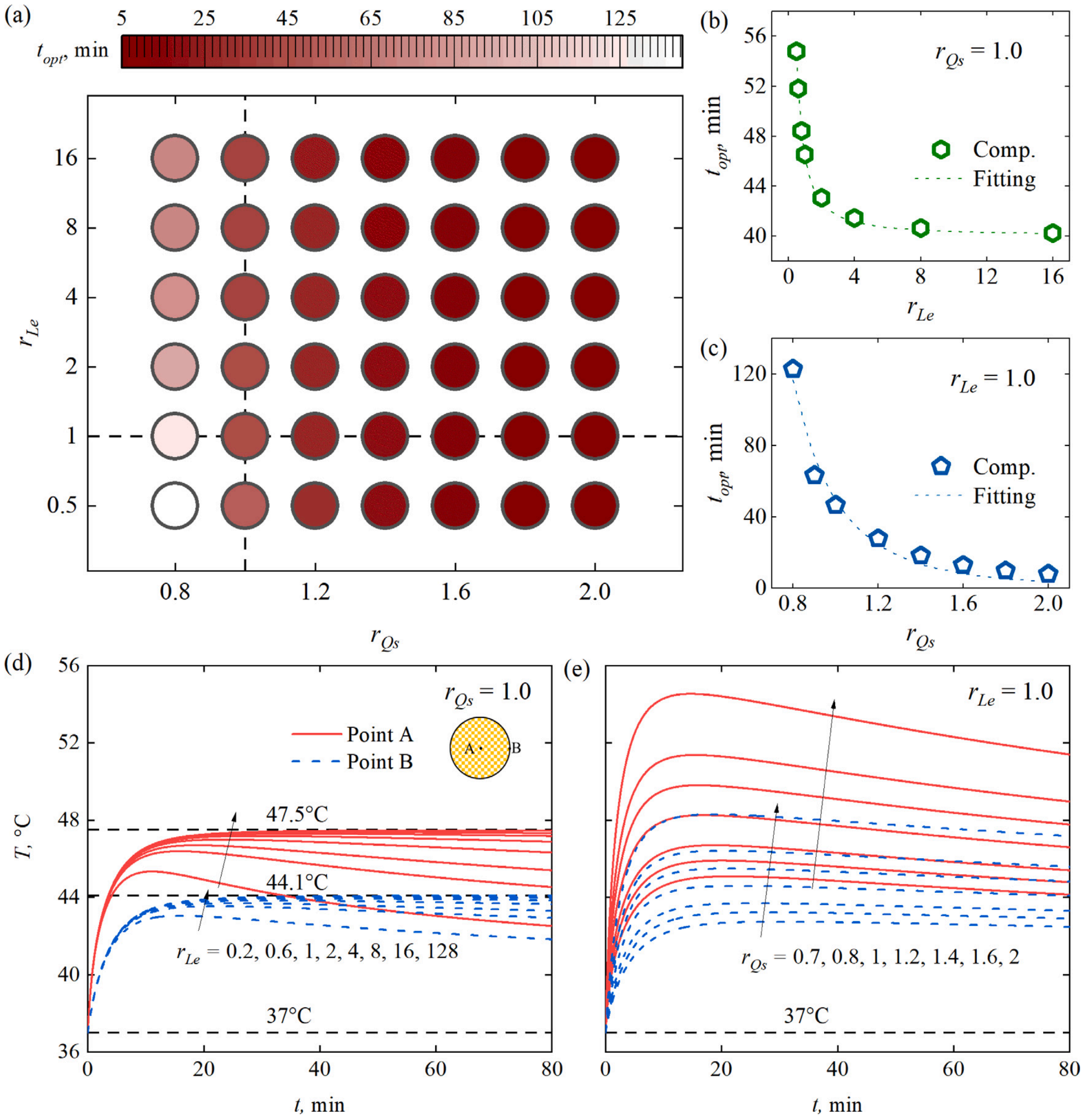

Fig. 4. Effect of Lewis number Le and heat source number Q_s on the optimal treatment time t_{opt} ((a)~(c)) and temperature at monitored points ((d) and (e)). (a) presents t_{opt} with the combination effect of Le and Q_s, while (b) and (c) are t_{opt} at $r_{Qs} = 1.0$ and $r_{Le} = 1.0$, respectively. The dash lines in (b) and (c) denote the corresponding fitting curve in power law functions, i.e., $t_{opt} = 2586Le^{-1.24} + 40.0$ min and $t_{opt} = 40544Q_s^{-3.84}$ min, respectively. The series of values for r_{Le} in (d) and r_{Qs} in (e) are used to clarify the lines in the direction of arrows.

in Fig. 5(c) to (f) that the spatial differences in MNP concentration lead to differences in temperature. They collectively generate downward buoyancy forces and cause a very slow flow (approximately 10^{-7} m/s), accompanied by a pair of counter-rotating vortices. The downward flow concurrently pulls the MNP, leading to the gradual downward movement of the concentration and temperature peaks. Furthermore, the combination of this slow convection with isotropic diffusivity of heat and MNP mass transfer produces slightly non-concentric patterns of the MNP concentration and temperature distribution, as also reported by Vijaybabu [70].

As a result, the MNP concentration and temperature at the tumor center become slightly smaller (about 0.2 °C at $t = 80$ min) if compared with those in the no-gravity scenario. The influence can be more obvious on the tumor boundary. For example, at $t = 80$ min, the temperature at the top point (point C) is about 0.6 °C lower, whereas it is about 0.5 °C higher at the bottom point (point D). Moreover, unlike in the no-gravity scenario, the temporal and spatial peak temperature no longer appears at the tumor center. Instead, a slightly (0.1%) lower peak value appears 0.5 mm (5% of the tumor diameter) below the tumor center at a slightly (1.6%) later time.

Fig. 6 presents the evolution of R_{CEM43} in the tumor and healthy tissues for the baseline case. It clearly reveals that, different from the no-gravity scenario, the gravity-induced downward MNP movement makes it impossible to achieve a perfect treatment (i.e., 100% tumor cells killed and no healthy tissue cell harmed). The tumor tissue starts to be ablated since $t = 11.7$ min, the same instant as that in the no-gravity scenario. However, as the treatment progresses to $t = 37.7$ min, the healthy tissue starts to be ablated from the bottom side of the tumor, while only 85.0% of the tumor cells are killed. When the tumor cells are just completely ablated at $t = 63.4$ min, about 21.3% healthy tissue cells have already been killed. It is also noted that the complete ablation time is 36.1% longer than the 46.6 min used in the no-gravity scenario. Therefore, obviously, the gravity effect deteriorates the treatment efficacy.

Fig. 7(a) and (b) present the distribution of required time for complete tumor cell ablation, t_{req}, and the corresponding ratio of damage in the healthy tissue, $R_{CEM43,h}$, respectively, in a parameter space

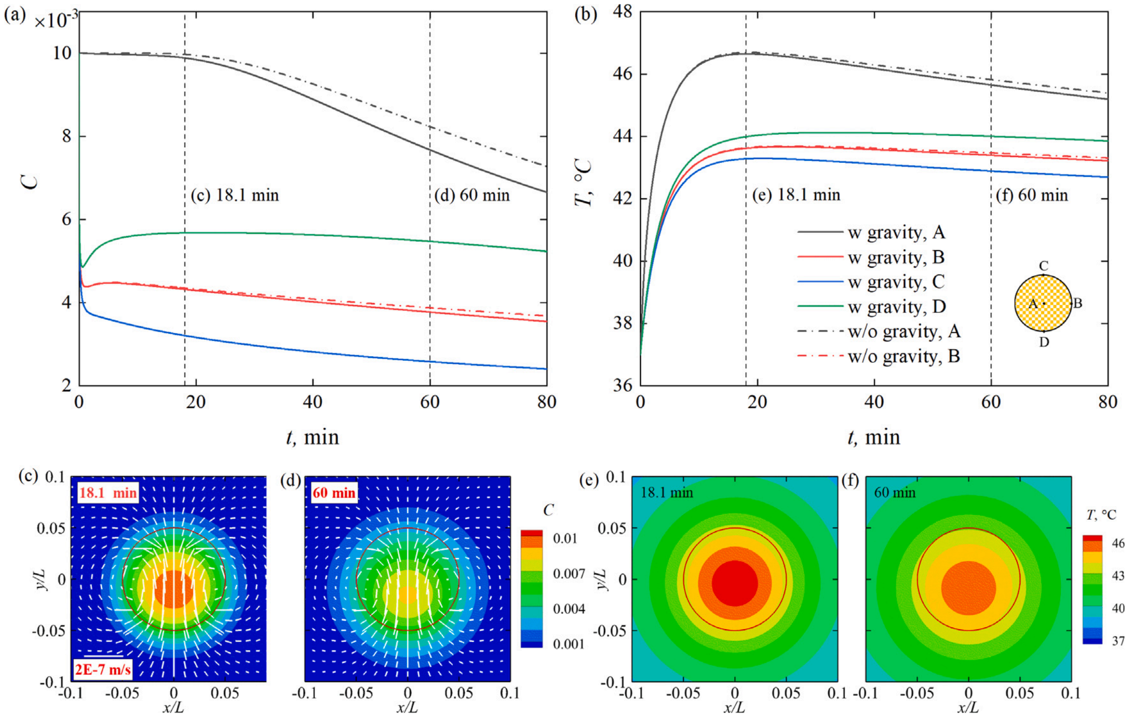

Fig. 5. Evolution of MNP concentration and temperature at the tumor center (point A), the rightmost point of the tumor (point B), its top point (point C), and its bottom point (point D), along with the distribution at some instants for the baseline case of with-gravity scenario (compared with the baseline case of no-gravity scenario). (c) and (d) denote the MNP concentration distribution at $t = 18.7$ min and $t = 60$ min, respectively; (e) and (f) denote the temperature distribution at $t = 18.7$ min and $t = 60$ min, respectively. For the no-gravity scenario, point B represents the situations of each boundary point. The white short lines in (c) and (d) denote the velocity, and the given length denotes the velocity magnitude of 2×10^{-7} m/s.

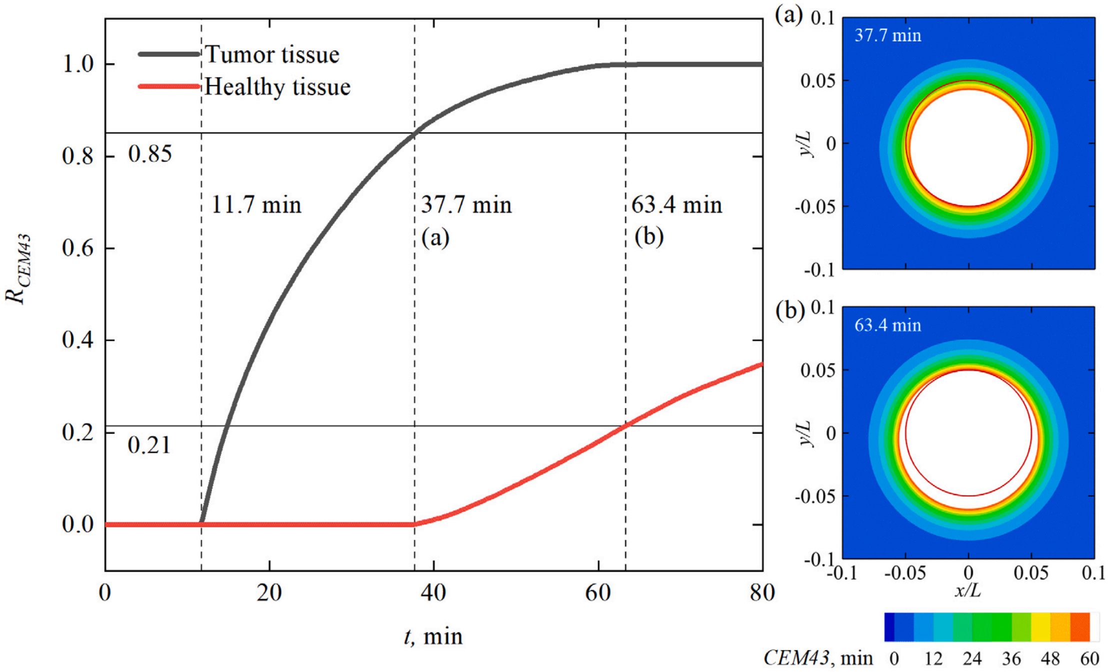

Fig. 6. (a) Evolution of R_{CEM43} in the tumor and healthy tissue for baseline case. (b) and (c) denote the distribution of $CEM43$ at $t = 37.7$ min and 63.4 min, respectively. The white region denotes the ablation part.

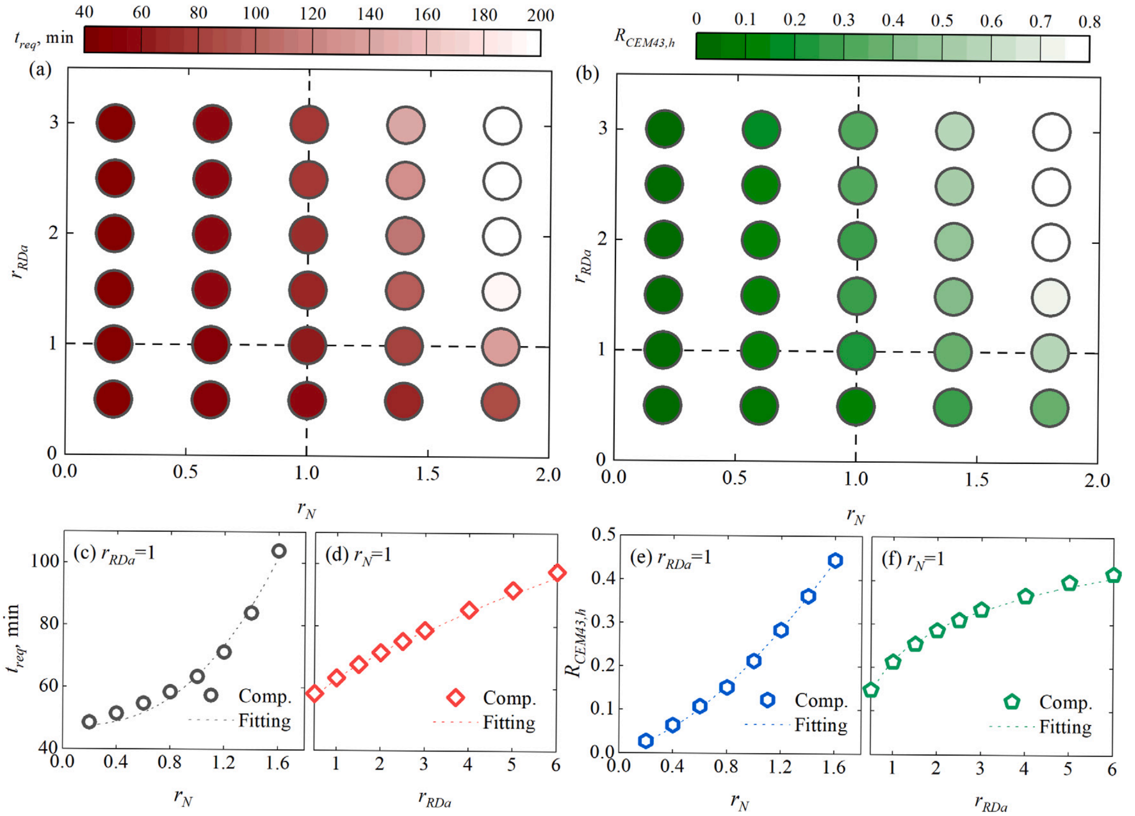

Fig. 7. Effect of buoyancy ratio N and Darcy ratio R_{Da} on (a) the required time t_{req} and (b) the corresponding injury $R_{CEM43,h}$. (c) and (d) denote t_{req} at r_N = 1.0 and r_{RDa} = 1.0, respectively, while (e) and (f) denote R_{CEM43} in the healthy tissue at r_N = 1.0 and r_{RDa} = 1.0, respectively. The dash lines in (c)~(f) denote the corresponding fitting curve in the power law functions, i.e., $t_{req} = 47.25 + 9.35 \times 10^{-3}|N|^{2.55}$ min in (c), $t_{req} = 46.6 + 6.05R_{Da}^{0.63}$ min in (d), $R_{CEM43,h} = 0.011 + 2.00 \times 10^{-3}|N|^{1.58}$ in (e), and $R_{CEM43,h} = 0.12R_{Da}^{0.39}$ in (f).

spanned by the buoyancy ratio N and the Darcy ratio R_{Da}, while the other parameters remain unchanged as in the baseline case. It is seen that in general both t_{req} and $R_{CEM43,h}$ increase with N and R_{Da}. If plotting the variations along the $r_{RDa} = 1.0$ line, Fig. 7(c) and (e) both show an obvious concave up, increasing curve. Along these curves, data fitting gives power laws to t_{req} and $R_{CEM43,h}$ against N as $t_{req} = 47.25 + 0.00935|N|^{2.55}$ min (with $R^2 = 0.987$) and $R_{CEM43,h} = 0.011 + 0.00200|N|^{1.58}$ (with $R^2 = 0.999$), respectively. The y-intercepts of these fitted curves suggest that, when $|N|$ approaches 0 meaning that the solutal buoyancy force diminishes, $t_{req} = 47.25$ min and $R_{CEM43,h} = 0.011$. Under this condition, only the mild thermal buoyancy force plays the role, t_{req} is slightly greater than $t_{opt} = 46.4$ min obtained in the no-gravity scenario, meanwhile $R_{CEM43,h}$ slightly deviates from zero. On the other hand, infinite $|N|$ leads to infinitely large t_{req} and pronounced $R_{CEM43,h}$, since a very large solutal buoyancy force drives all MNPs away from the tumor almost immediately.

If plotting the variations along the $r_N = 1.0$ line, Fig. 7(d) and (f) both show a slightly concave down, increasing curve. Along these curves, data fitting gives power laws to t_{req} and $R_{CEM43,h}$ against R_{Da} as $t_{req} = 46.6 + 6.05R_{Da}^{0.63}$ min (with $R^2 = 0.998$) and $R_{CEM43,h} = 0.12R_{Da}^{0.39}$ (with $R^2 = 0.992$). As R_{Da} approaches 0, the flow resistance in the tumor is extremely large, resulting in no interstitial flow. As such, t_{req} and $R_{CEM43,h}$ are identical to the results obtained in the baseline case for the no-gravity scenario. In this case, we have $t_{req} = t_{opt} = 46.6$ min, and no injury occurs in the healthy tissue. As R_{Da} increases, however, the interstitial fluid moves in the tumor under the gravity effect, so do the carried MNPs. This movement results in the unbalanced MNP distribution (as can be confirmed later in Fig. 9(h)) and is hence responsible for the increase of t_{req} and $R_{CEM43,h}$.

If considering the combined influence of the buoyancy ratio N and the Darcy ratio R_{Da}, more general power laws can be obtained as $t_{req} = 0.00165|N|^{2.69}R_{Da}^{0.80} + 46.6$ min (with $R^2 = 0.990$) and $R_{CEM43,h} = 0.00143|N|^{1.47}R_{Da}^{0.43}$ (with $R^2 = 0.998$).

Fig. 8(a) presents the evolution of R_{CEM43} in both tumor and healthy tissue at three selected buoyancy ratios, i.e., r_N = 0.4, 1.0, and 1.6. The deviation among these three cases becomes pronounced after about 30 min. As r_N increases, the tumor killing process slows down, and the time required to destroy all the tumor cells is significantly lengthened from $t_{req} = 51.4$ min (at $r_N = 0.4$) to 104.0 min (at $r_N = 1.6$), more than doubled. Meanwhile, the ablation of healthy tissue starts earlier, from 43.9 min at $r_N = 0.4$ to 34.2 min at $r_N = 1.6$, reduced by 22%. These observations are not surprising since the increase in solutal buoyancy force makes the downward drift of MNPs faster and their moving across the bottom side of the tumor earlier. This influence is also reflected by the temperature evolution presented in Fig. 8(b), where the temperature difference between the top and bottom points (i.e., points C and D) becomes more and more obvious with the increase of r_N.

Fig. 8(c)~(k) further compare the MNP concentration, temperature, and $CEM43$ distributions among the three selected buoyancy ratios at $t = 50$ min, when the deviations are pronounced. It is seen that, as r_N increases, the contour patterns of the MNP concentration and the resulting temperature move further downwards. These downward movements result in the deterioration of the treatment efficacy, i.e., R_{CEM43} in tumor reduces from 0.996 (at $r_N = 0.4$) to 0.923 (at $r_N = 1.6$), while $R_{CEM43,h}$ in healthy tissue increases from 0.056 to 0.117. Interestingly, the downward movement of MNPs induces a secondary flow, i.e., a pair of vortices, which also slightly affects the MNP and temperature distributions in the horizontal direction.

Similarly, Fig. 9 presents the evolution of R_{CEM43} in the tumor and healthy tissues and temperature at monitored points, as well as the distributions of MNP concentration, temperature, and $CEM43$ at $t = 50$ min for three different Darcy number ratios, i.e., r_{RDa} = 0.5, 1.0 and

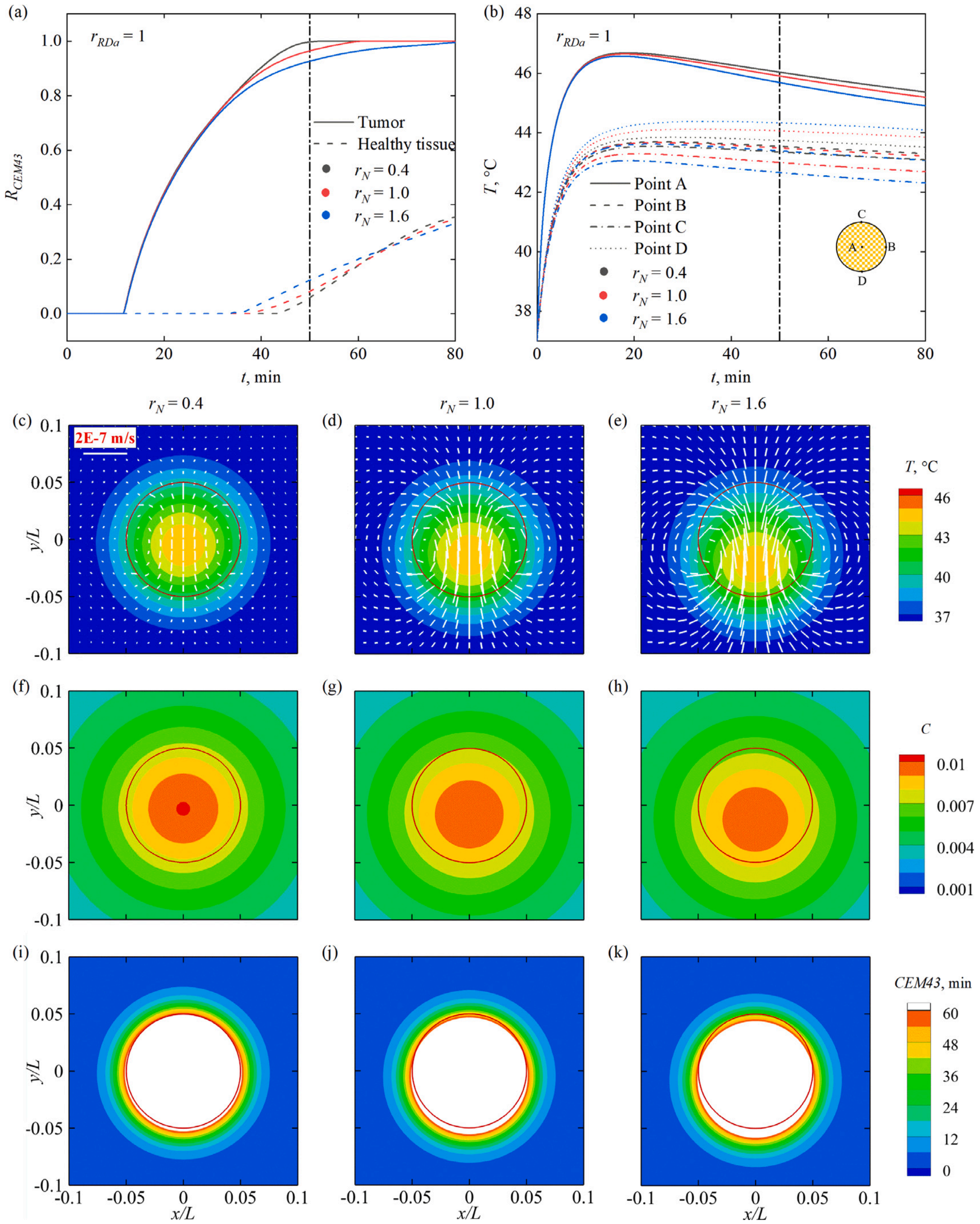

Fig. 8. Evolution of R_{CEM43} in both tumor and healthy tissue (a), and evolution of T at monitored points (b) as buoyancy ratio N varies. (c)~(k) are MNP concentration, temperature distribution, and $CEM43$ distribution for r_N = 0.4, 1.0, and 1.6, respectively, at treatment time t = 50 min. The white short lines in (c)~(e) denote the velocity, and the given length denotes the velocity magnitude of 2×10^{-7} m/s. The red circle denotes the tumor boundary, while the white region denotes the destroyed part. (For interpretation of the references to color in this figure legend, the reader is referred to the web version of this article.)

2.0. It is seen that, compared to r_N, r_{RDa} has a similar but less effect on the above quantities. Therefore, the treatment efficacy worsens as r_{RDa} increases. Specifically, by increasing r_{RDa} from 0.5 to 2.0, the time required t_{req} for complete ablation of tumor cells extends by 22.7%, while the time for starting ablation of the healthy tissue is advanced by 8.1%.

4. Conclusion

In this study, we established an LBM based computational framework for the simulation of magnetic hyperthermia treatment. This framework is capable of simulating multiphysics phenomena involving flow in porous medium, heat and mass transfer, magnetics and nanofluid. The simulation can reveal the temporal and spatial evolutions of MNP concentration and temperature, as well as interstitial tissue fluid flow in both tumor and surrounding healthy tissue. The efficacy of magnetic hyperthermia therapy is assessed via the $CEM43$ model, wherein cell death is determined by both temperature and duration of heating.

With this framework, a simple tumor model, i.e., a tumor of circular shape surrounded by healthy tissue, was simulated under various conditions. The discussions of simulation results are grouped in two

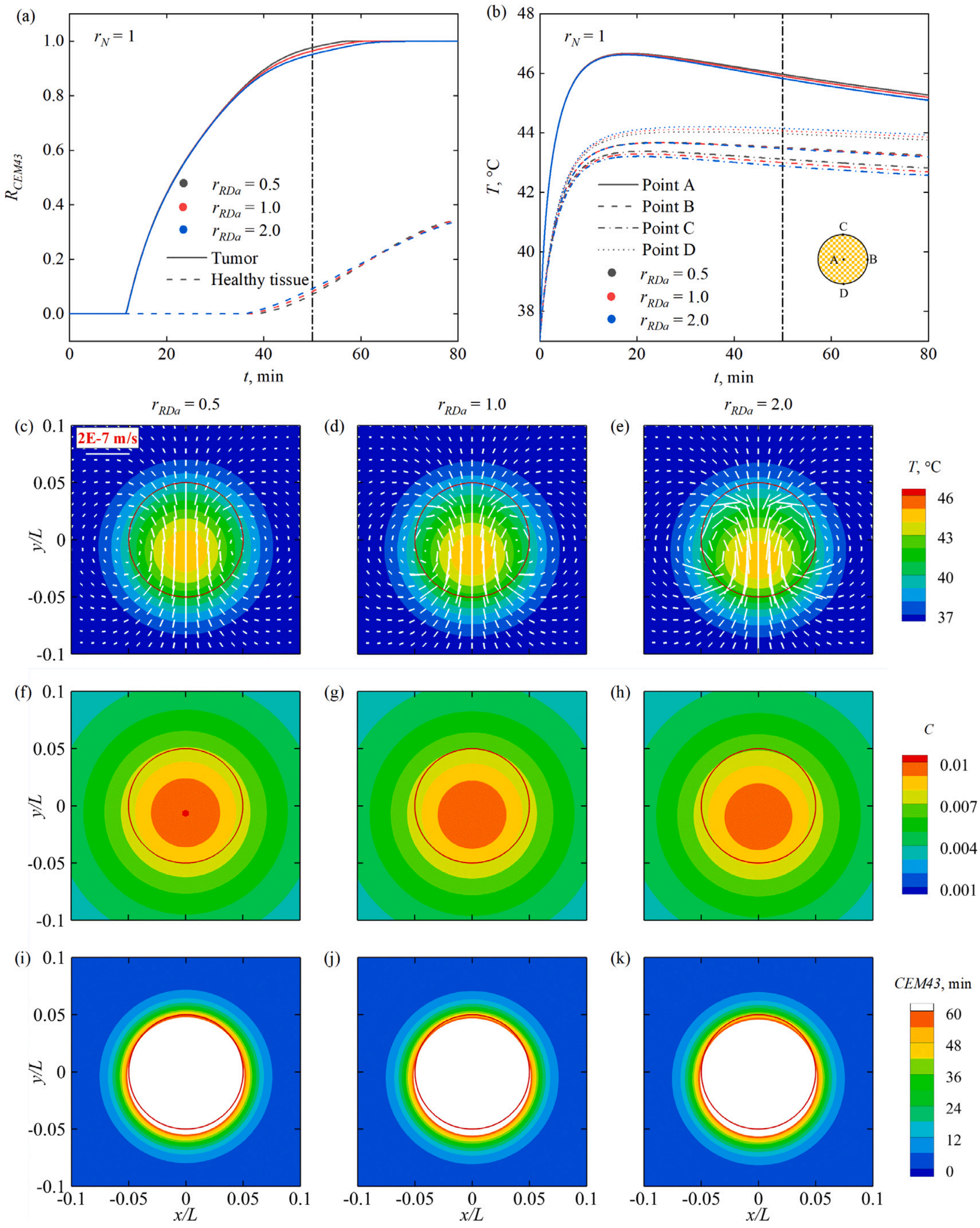

Fig. 9. Evolution of R_{CEM43} in both tumor and healthy tissue (a), and evolution of T at monitored points (b) as Darcy ratio R_{Da} varies. (c)~(k) are MNP concentration, temperature distribution, and $CEM43$ distribution for r_{RDa} = 0.5, 1.0, and 2.0, respectively, at treatment time t = 50 min. The white short lines in (c)~(e) denote the velocity, and the given length denotes the velocity magnitude of 2×10^{-7} m/s. The red circle denotes the tumor boundary, while the white region denotes the destroyed part. (For interpretation of the references to color in this figure legend, the reader is referred to the web version of this article.)

scenarios, depending on whether the gravity is considered or not. In the scenario when the gravity is ignored, the tissue flow remains stationary, and hence both the MNP concentration and temperature concentrically spread from the tumor center. The optimal treatment time t_{opt} decreases with both the Lewis number Le and the heat source number Q_s, which follows a power law, i.e., $t_{opt} = (4097386Le^{-1.35} + 20714)Q_s^{-3.58}$ in the unit of minute. Note that in our previous work [63] we treated the MNPs as "frozen" due to a high Le value of 125 being adopted. Our present study suggests that, although the effect of Le is relatively small, especially at large values, the MNP diffusion during the heating process should be taken into account for more accurate assessment of magnetic hyperthermia treatment.

In the scenario where the gravity is introduced, the treatment efficacy deteriorates due to the buoyancy flow-induced MNP movement. It significantly extends the time required t_{req} for completely killing the tumor cells and meanwhile causes unignorable damages in healthy tissue. It was found that t_{req} and the corresponding damage in healthy tissue $R_{CEM43,h}$ both increase with the buoyancy ratio N and Darcy ratio R_{Da}, also following useful power laws, i.e., $t_{req} = 0.00165|N|^{2.69}R_{Da}^{0.80} + 46.6$ in the unit of minute and $R_{CEM43,h} = 0.00143|N|^{1.47}R_{Da}^{0.43}$.

The results highlight the significant impact of gravity, which should be considered when planning magnetic hyperthermia treatments. In practice, the influence of gravity can be mitigated through MNP coating techniques, such as using chitosan and natural organic polymers, to reduce both MNP sedimentation [45] and toxicity [9,71,72]. Typically, the treatment duration for magnetic hyperthermia is around several tens of minutes [11,73]. A duration that is too short can complicate the accurate operation of the treatment, while an excessively long session is inefficient and may lead to operator fatigue. Therefore, precise operation and time consumption need to be well balanced.

Although multiphysics models have been integrated into the framework, magnetic hyperthermia remains a highly complex procedure that requires further development. Due to simplifications in configuration and limitations in length, numerous practical investigations should be addressed in the near future, including the variations in properties in the tissues, the spatially nonuniform initial distribution of MNP, and the irregular shape of tumors. Despite the two-dimensional configuration, the study provides valuable insights and a deeper understanding of the heating mechanism and tumor ablation in magnetic hyperthermia treatment, offering significant predictions and recommendations for therapy. Furthermore, it is noteworthy that clinical treatment data should be incorporated soon. Although finding the related medical experiments is challenging, comparisons with them are crucial for further framework development.

CRediT authorship contribution statement

Qian Jiang: Writing – review & editing, Writing – original draft, Visualization, Validation, Software, Methodology, Investigation, Formal analysis. **Feng Ren:** Writing – review & editing, Software, Methodology. **Chenglei Wang:** Writing – review & editing, Methodology. **Zhaokun Wang:** Writing – review & editing, Methodology. **Gholamreza Kefayati:** Writing – review & editing. **Sasa Kenjeres:** Writing – review & editing. **Kambiz Vafai:** Writing – review & editing. **Xinguang Cui:** Writing – review & editing. **Yang Liu:** Writing – review & editing, Supervision. **Hui Tang:** Writing – review & editing, Supervision, Methodology, Investigation, Funding acquisition, Conceptualization.

Declaration of competing interest

The authors declare the following financial interests/personal relationships which may be considered as potential competing interests: Dr Tang Hui reports financial support was provided by Research Grants Council of Hong Kong. If there are other authors, they declare that they have no known competing financial interests or personal relationships that could have appeared to influence the work reported in this paper.

Acknowledgment

This study was financially supported by the Research Grants Council of Hong Kong under General Research Fund (Project No. 15214418).

Appendix A. Lattice Boltzmann method

The LBM is a relatively new computational fluid dynamics (CFD) approach for simulating fluid flow and heat/mass transfer. Unlike traditional CFD methods, which numerically solve the conservation equations of macroscopic properties, LBM models fluid particles by distribution functions through consecutive streaming and collision processes over square lattices [74–76]. Zhang [37] was probably the first to apply the LBM to solving PBHTE, successfully demonstrating the capability of LBM in simulating bioheat problems. This mesoscopic approach was then widely applied to bioheat studies [20,77,78]. In the present work, D2Q9 (i.e., two-dimensional nine-discrete-velocity) and D2Q5 (i.e., two-dimensional five-discrete-velocity) MRT (i.e., multiple-relaxation-time [79]) LBM schemes are employed to solve the vector field (flow field) and scalar fields (temperature field and concentration field), respectively, governed by Eq. (1) [40,57].

The discrete D2Q9 MRT-LBM equation for fluid field with second-order accuracy is written as

$$\mathbf{f}(x_k+\mathbf{e}\delta_t,t_n+\delta_t)-\mathbf{f}(x_k,t_n)=-\mathbf{M}^{-1}\mathbf{\Lambda}[\mathbf{m}-\mathbf{m}^{(eq)}]|_{(x_k,t_n)}+\mathbf{M}^{-1}\delta_t(1-\frac{\mathbf{\Lambda}}{2})\mathbf{S}, \tag{A.1}$$

where $\mathbf{f}(x_k,t_n)=(f_0(x_k,t_n),f_1(x_k,t_n),\dots,f_8(x_k,t_n))^T$ is particle distribution function vectors at time t_n and node x_k for fluid field. $\mathbf{m}$ and $\mathbf{m}^{(eq)}$ are the vectors for the distribution function and the responding equilibrium distribution function, respectively. $\mathbf{e}$ denotes unit velocities along 9 discrete directions

$$e_i=\begin{cases}(0,0), & i=0\\ (\cos[(i-1)\pi/2],\sin[(i-1)\pi/2])c, & i=1\sim 4\\ (\cos[(2i-9)\pi/4],\sin[(2i-9)\pi/4])\sqrt{2}c, & i=5\sim 8,\end{cases} \tag{A.2}$$

where $c=\delta_x/\delta_t$ is the lattice speed, which is 1 since $\delta_x=\delta_t$ in the present MRT model. $\mathbf{M}$ is a 9×9 orthogonal transformation matrix, as

$$\mathbf{M}=\begin{pmatrix}1&1&1&1&1&1&1&1&1\\-4&-1&-1&-1&-1&2&2&2&2\\4&-2&-2&-2&-2&1&1&1&1\\0&1&0&-1&0&1&-1&-1&1\\0&-2&0&2&0&1&-1&-1&1\\0&0&1&0&-1&1&1&-1&-1\\0&0&-2&0&2&1&1&-1&-1\\0&1&-1&1&-1&0&0&0&0\\0&0&0&0&0&1&-1&1&-1\end{pmatrix}. \tag{A.3}$$

$\mathbf{\Lambda}$ is a diagonal relaxation matrix and defined as

$$\mathbf{\Lambda}=\mathrm{diag}(1,1.1,1.1,1,1.2,1,1.2,1/\tau_\upsilon,1/\tau_\upsilon), \tag{A.4}$$

in which τ_υ can be recovered to the viscosity of nanofluid by Chapman–Enskog analysis on Eq. (1) as

$$\upsilon_{nf}=c_s^2(\tau_\upsilon-0.5)\delta_t. \tag{A.5}$$

$\mathbf{S}$ represents the external force in the momentum space and is directly related to the body force $\mathbf{F}$ in the governing Eq. (1)(b).

The discrete D2Q5 MRT-LBM equations for temperature and concentration fields are formulated as

$$\mathbf{g}(x_k+\mathbf{e}\delta_t,t_n+\delta_t)-\mathbf{g}(x_k,t_n)=-\mathbf{N}^{-1}\mathbf{\Theta}[\mathbf{n_g}-\mathbf{n_g}^{(eq)}]|_{(x_k,t_n)}+\mathbf{N}^{-1}\delta_t\mathbf{\Psi}, \tag{A.6a}$$

$$\mathbf{h}(x_k+\mathbf{e}\delta_t,t_n+\delta_t)-\mathbf{h}(x_k,t_n)=-\mathbf{N}^{-1}\mathbf{\Upsilon}[\mathbf{n_h}-\mathbf{n_h}^{(eq)}]|_{(x_k,t_n)}, \tag{A.6b}$$

where $\mathbf{g}(x_k,t_n)$ and $\mathbf{h}(x_k,t_n)$ are distribution function vectors at time t_n and node x_k for temperature and concentration, respectively. $\mathbf{n}$ and $\mathbf{n}^{(eq)}$ denote the vectors for the distribution function and the corresponding equilibrium distribution function, respectively, where subscribe "g" represents the temperature field and "h" denotes the concentration field. $\mathbf{e}$ describes unit velocities along 5 discrete directions

$$e_i=\begin{cases}(0,0), & i=0\\ (\cos[(i-1)\pi/2],\sin[(i-1)\pi/2])c, & i=1\sim 4.\end{cases} \tag{A.7}$$

$\mathbf{N}$ is a 5×5 orthogonal transformation matrix, as

$$\mathbf{N}=\begin{pmatrix}1&1&1&1&1\\0&1&0&-1&0\\0&0&1&0&-1\\-4&1&1&1&1\\0&1&-1&1&-1\end{pmatrix}. \tag{A.8}$$

$\mathbf{\Theta}$ and $\mathbf{\Upsilon}$ are the diagonal relaxation matrix

$$\mathbf{\Theta}=\mathrm{diag}(1,1/\tau_T,1/\tau_T,1.5,1.5), \tag{A.9a}$$

$$\mathbf{\Upsilon}=\mathrm{diag}(1,1/\tau_C,1/\tau_C,1.5,1.5), \tag{A.9b}$$

Table A.1
Sensitivity studies on computational domain size, grid number, and time step.

	L/d_{tum}	t, min	T_A, °C	T_D, °C	Err_A, %	Err_D, %
Domain size	5	30	46.40	43.56	0.09	1.28
		60	45.64	43.29	0.03	1.61
	10	30	46.44	44.12	0.13	0.13
		60	45.65	44.00	0.12	0.12
	20	30	46.38	44.06	–	–
		60	45.59	43.95	–	–
	$NX \times NY$	t, min	T_A, °C	T_D, °C	Err_A, %	Err_D, %
Grid number	200 × 200	30	46.38	44.32	1.46	0.44
		60	45.56	44.14	1.94	0.33
	400 × 400	30	46.44	44.12	0.02	0.05
		60	45.65	44.00	0.01	0.04
	600 × 600	30	46.44	44.10	–	–
		60	45.64	43.98	–	–
	dt, $\times 10^{-4}$ s	t, min	T_A, °C	T_D, °C	Err_A, %	Err_D, %
Time step	19.0	30	46.34	44.29	0.22	0.38
		60	45.53	44.12	0.26	0.27
	9.5	30	46.44	44.12	0.06	0.16
		60	45.65	44.00	0.09	0.11
	4.8	30	46.47	44.05	–	–
		60	45.69	43.95	–	–

where τ_T is associated with the effective thermal diffusivity (in the temperature field), while τ_C is linked to the effective concentration diffusivity (in the concentration field), as

$$\alpha_e = \sigma c_{sT}^2(\tau_T - 0.5)\delta_t,\ D_e = \phi c_{sT}^2(\tau_C - 0.5)\delta_t. \tag{A.10}$$

The vector $\boldsymbol{\Psi}$ denotes the heat source, which corresponds to the heat source term Q in the governing equation (1) (c). More details about the D2Q5 MRT-LBM can be found in [40,57].

In this study, the halfway bounce-back scheme is applied to the stationary wall, while the anti-bounce-back scheme is adopted for the constant values of the thermal and solutal boundaries. Continuous velocity, temperature, and concentration are imposed at the interface between the healthy tissue and the tumor.

A spatial and temporal resolution test was conducted, encompassing the categories of computational domain size, grid number, and time step. The baseline case with gravity was chosen as an example, and temperature values at specific points (Point A and Point D) were monitored. The results are presented in Table A.1, indicating that a computational domain size of $10d_{tum} \times 10d_{tum}$, a grid number of 400 × 400, and the time step 9.5×10^{-4} are suitable in this study.

Since the magnetic hyperthermia problem governed by Eq. (1) can be viewed as a double-diffusive convection problem in porous media, a validation study was conducted using a typical porous double-diffusive convection scenario. The comparison of velocity and temperature profiles with those obtained from Ref. [57] on the variation of buoyancy ratio N is presented in Fig. A.1. The results demonstrate a good agreement between the present framework and the reference study, indicating the validity of the current framework.

Appendix B. Alternating Lorentz force

The external Lorentz force induced by the AMF is an alternating force. However, due to the significant difference in time scales between the magnetic field (approximately 100~400 kHz) and the flow field (with the reference frequency v_f/L^2 being much less than 1 s^{-1}) in this study, direct calculation can lead to an overwhelming amount of computational workload. Therefore, it is necessary to simplify this alternating Lorentz force into a steady model. The derivation is presented as follows.

A homogeneous sinusoidal AMF at an angle α to the x-axis is considered. The angular frequency is denoted by ω, and the magnetic intensity is $B = (B_x, B_y)$ (with its amplitude represented as $B_0 = (B_{x0}, B_{y0})$). Therefore, the alternating Lorentz force acting on the x-axis can be expressed as

$$\begin{aligned} F_{Mx} &= -\sigma_{Enf} B_y^2 u + \sigma_{Enf} B_x B_y v \\ &= -\sigma_{Enf} B_{y0}^2 \sin^2 \omega t u + \sigma_{Enf} B_{x0} B_{y0} \sin^2 \omega t v \\ &= \sin^2 \omega t(-\sigma_{Enf} B_{y0}^2 u + \sigma_{Enf} B_{x0} B_{y0} v). \end{aligned} \tag{B.1}$$

We assume a period of $[0, nT]$, where n cycles of magnetic oscillation are included and the velocity (u, v) is approximated as constant. The integration of the Lorentz force over this period is given by

$$\begin{aligned} \int_0^{nT} F_{Mx} dt = \int_0^{nT} \sin^2 \omega t(-\sigma_{Enf} B_{y0}^2 u + \sigma_{Enf} B_{x0} B_{y0} v) dt \\ &= (-\sigma_{Enf} B_{y0}^2 u + \sigma_{Enf} B_{x0} B_{y0} v) \int_0^{nT} \sin^2 \omega t dt \\ &= (-\sigma_{Enf} B_{y0}^2 u + \sigma_{Enf} B_{x0} B_{y0} v) \int_0^{nT} \frac{1}{2}(1 - \cos 2\omega t) dt \\ &= (-\sigma_{Enf} B_{y0}^2 u + \sigma_{Enf} B_{x0} B_{y0} v) \cdot \frac{1}{2} nT \\ &= \frac{1}{2} \int_0^{nT} (-\sigma_{Enf} B_{y0}^2 u + \sigma_{Enf} B_{x0} B_{y0} v) dt. \end{aligned} \tag{B.2}$$

Consequently, the alternating Lorentz force in Eq. (B.1) can be substituted by

$$F_{Mx} = -\sigma_{Enf} \left(\frac{1}{\sqrt{2}} B_0 \right)^2 \sin^2 \alpha u + \sigma_{Enf} \left(\frac{1}{\sqrt{2}} B_0 \right)^2 \sin \alpha \cos \alpha v. \tag{B.3}$$

This means that the alternating Lorentz force can be considered equivalent to a steady Lorentz force, where the amplitude of steady magnetic intensity is $1/\sqrt{2}$ of that in the alternating magnetic field.

Similarly, the alternating Lorentz force on the y-axis is given by

$$\begin{aligned} F_{My} &= -\sigma_{Enf} B_x^2 v + \sigma_{Enf} B_x B_y u \\ &= -\sigma_{Enf} B_{y0}^2 \cos^2 \omega t v + \sigma_{Enf} B_{x0} B_{y0} \sin^2 \omega t u \\ &= \sin^2 \omega t(-\sigma_{Enf} B_{x0}^2 v + \sigma_{Enf} B_{x0} B_{y0} u). \end{aligned} \tag{B.4}$$

The same process can be carried out along the y-axis to establish the corresponding equivalence relation.

A validation process, which consists of two steps, is conducted to test the feasibility of this approach. The first step aims to validate the Lorentz force exerted by the steady magnetic field. The second step aims to confirm the equivalence relation between the steady and alternating Lorentz forces.

The schematic shown in Fig. B.1(a) is used in the first step. This is a buoyancy-driven natural convection problem influenced by a uniform steady magnetic field [80]. The homogeneous nanofluid, a mixture of water and Al_2O_3 nanoparticles, fills the square enclosure with all the boundaries fixed. The horizontal walls are adiabatic, while the left and right walls maintain constant temperatures (T_h and T_l, respectively).

The velocity and temperature profiles are presented in Fig. B.1(b) and (c), respectively, with the fixed Rayleigh number ($Ra = 10^5$) and nanoparticle volume fraction ($\phi = 0.03$). The simulation results demonstrate good agreement with the reference study [80] for different Hartman numbers.

Next, the velocity and temperature fields obtained from the natural convection simulation with the steady magnetic field are extracted and imported into an identical enclosure but with an AMF. Specifically, the intensity amplitude of the AMF is $\sqrt{2}$ times greater than that of the steady magnetic field. As revealed in Fig. B.2, the flow and temperature fields remain unchanged after 2×10^6 cycles of magnetic oscillation. This observation confirms the suitability and efficiency of the proposed equivalent model. Therefore, in the present work, the steady magnetic Lorentz force model is employed to substitute for the calculation of the alternating Lorentz force.

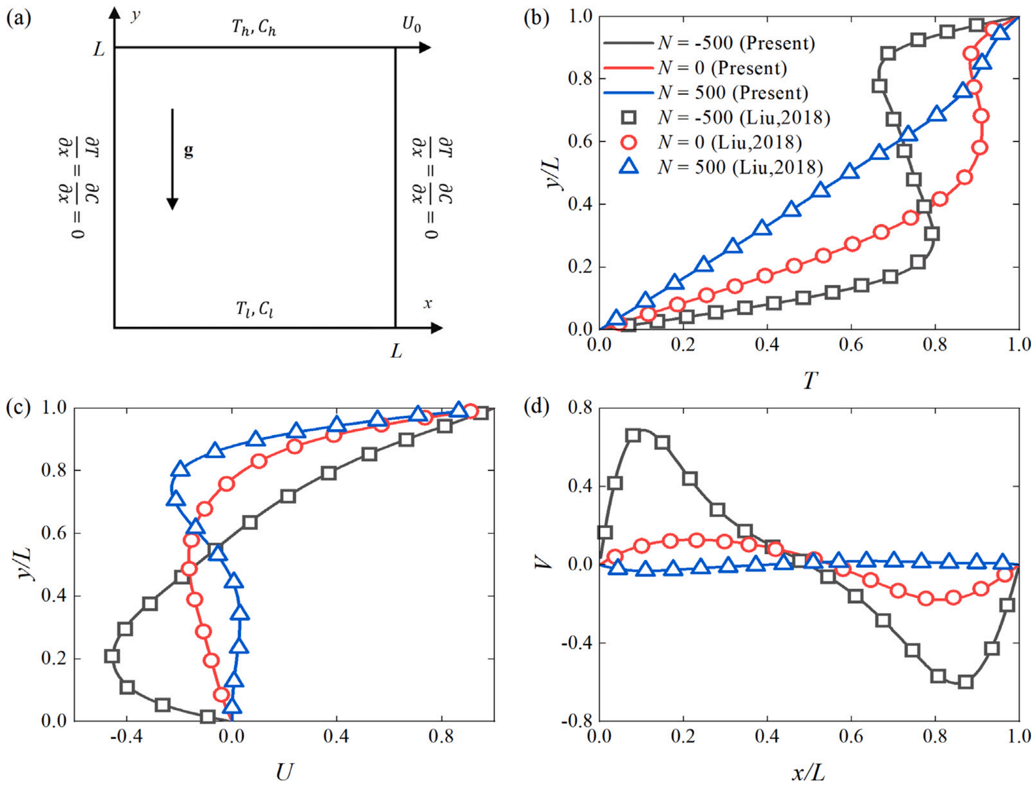

Fig. A.1. Validation of LBM framework on double-diffusive convection problem in porous media. (a) the schematic of the problem; (b) temperature profile at $x/L = 0.5$; (c) horizontal velocity profile at $x/L = 0.5$; (d) vertical velocity profile at $y/L = 0.5$.

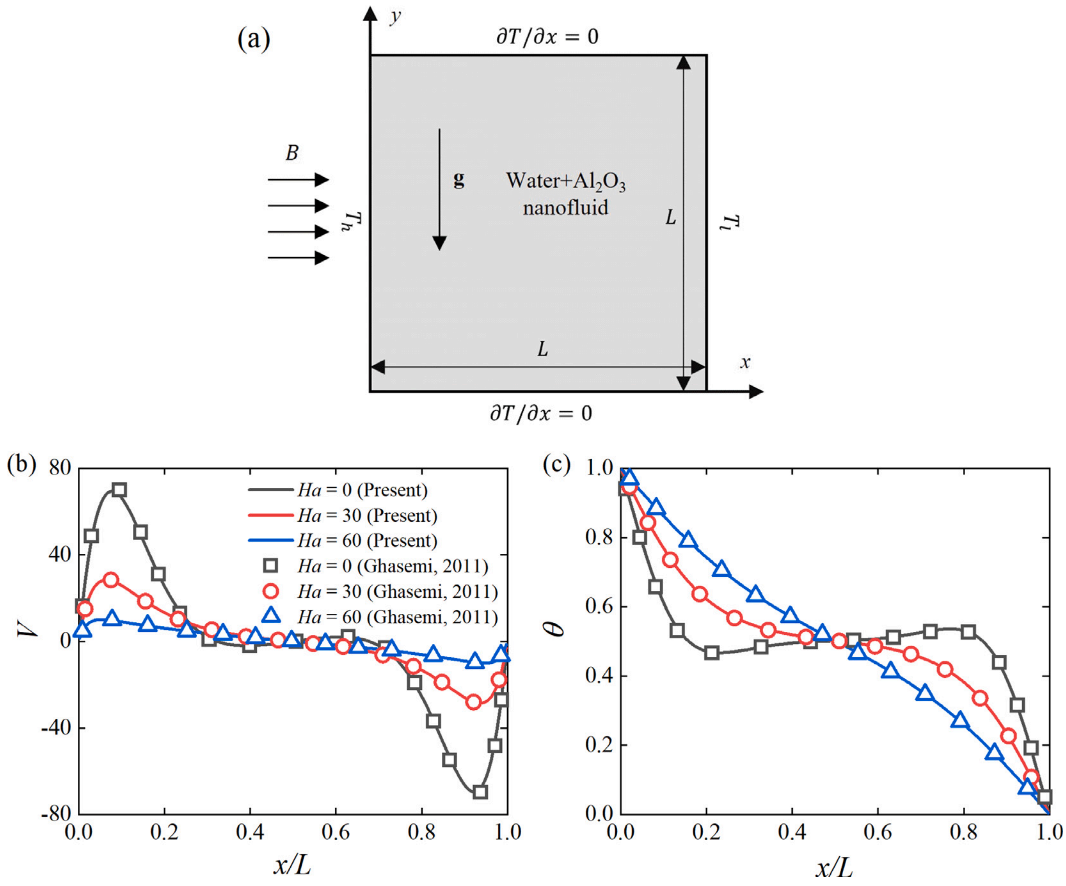

Fig. B.1. Validation on steady Lorentz force by the natural convection problem. (a) Schematic of the problem; (b) the vertical velocity profile on $y/L = 0.5$; (c) temperature on $y/L = 0.5$.

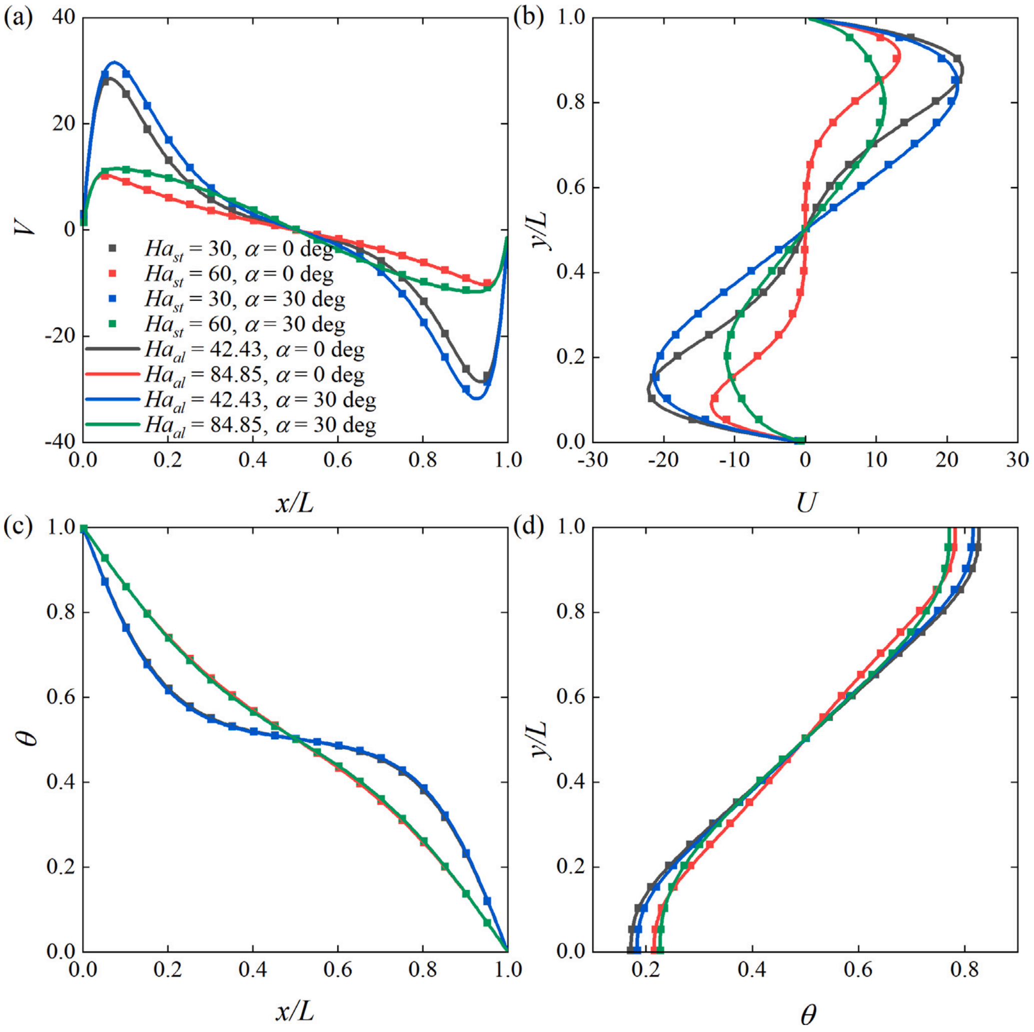

Fig. B.2. Validation on the high-frequency alternating Lorentz force. (a) vertical velocity at $y = 0.5$, (b) horizontal velocity profile at $x/L = 0.5$, (c) temperature profile at $y/L = 0.5$, (d) temperature profile at $x/L = 0.5$.

Data availability

Data will be made available on request.

References

[1] S. Sharma, N. Shrivastava, F. Rossi, N.T.K. Thanh, et al., Nanoparticles-based magnetic and photo induced hyperthermia for cancer treatment, Nano Today 29 (2019) 100795.

[2] V. Vilas-Boas, F. Carvalho, B. Espiña, Magnetic hyperthermia for cancer treatment: main parameters affecting the outcome of in vitro and in vivo studies, Molecules 25 (12) (2020) 2874.

[3] J. Ma, X. Yang, Y. Sun, J. Yang, Theoretical investigation on the thermo-mechanical responses of the human skin during thermal therapy, Int. J. Mech. Sci. 161 (2019) 105041.

[4] S. Imanlou, K. Vafai, Hyperthermia applications in cardiovascular and cancer therapy treatments, 2024.

[5] A. Singh, N. Kumar, Estimation of the injection criteria for magnetic hyperthermia therapy based on tumor morphology, Biomed. Phys. Eng. Express 10 (5) (2024) 055017.

[6] R. Roohi, M. Heydari, Z. Avazzadeh, Optimal control of hyperthermia thermal damage based on tumor configuration, Results Phys. 23 (2021) 103992.

[7] E.A. Périgo, G. Hemery, O. Sandre, D. Ortega, E. Garaio, F. Plazaola, F.J. Teran, Fundamentals and advances in magnetic hyperthermia, Appl. Phys. Rev. 2 (4) (2015) 041302.

[8] J. Jose, R. Kumar, S. Harilal, G.E. Mathew, D.G.T. Parambi, A. Prabhu, M. Uddin, L. Aleya, H. Kim, B. Mathew, et al., Magnetic nanoparticles for hyperthermia in cancer treatment: an emerging tool, Environ. Sci. Pollut. Res. 27 (16) (2020) 19214–19225.

[9] D. Karponis, M. Azzawi, A. Seifalian, An arsenal of magnetic nanoparticles; perspectives in the treatment of cancer, Nanomedicine 11 (16) (2016) 2215–2232.

[10] E. Kosari, K. Vafai, Transport and dynamic analysis of magnetic nanoparticles in brain microvascular vessels, Phys. Fluids 33 (8) (2021) 081907.

[11] D. Chang, M. Lim, J.A. Goos, R. Qiao, Y.Y. Ng, F.M. Mansfeld, M. Jackson, T.P. Davis, M. Kavallaris, Biologically targeted magnetic hyperthermia: potential and limitations, Front. Pharmacol. 9 (2018) 831.

[12] O.A. Aladesuyi, O.S. Oluwafemi, The role of magnetic nanoparticles in cancer management, Nano- Struct. Nano- Objects 36 (2023) 101053.

[13] M. Suto, Y. Hirota, H. Mamiya, A. Fujita, R. Kasuya, K. Tohji, B. Jeyadevan, Heat dissipation mechanism of magnetite nanoparticles in magnetic fluid hyperthermia, J. Magn. Magn. Mater. 321 (10) (2009) 1493–1496.

[14] R.E. Rosensweig, Heating magnetic fluid with alternating magnetic field, J. Magn. Magn. Mater. 252 (2002) 370–374.

[15] G. Singh, N. Kumar, P.K. Avti, Computational evaluation of effectiveness for intratumoral injection strategies in magnetic nanoparticle assisted thermotherapy, Int. J. Heat Mass Transfer 148 (2020) 119129.

[16] K. Mahmoudi, A. Bouras, D. Bozec, R. Ivkov, C. Hadjipanayis, Magnetic hyperthermia therapy for the treatment of glioblastoma: a review of the therapy's history, efficacy and application in humans, Int. J. Hyperth. 34 (8) (2018) 1316–1328.

[17] I. Raouf, S. Khalid, A. Khan, J. Lee, H.S. Kim, M.-H. Kim, A review on numerical modeling for magnetic nanoparticle hyperthermia: Progress and challenges, J. Therm. Biol. 91 (2020) 102644.

[18] K. Maier-Hauff, F. Ulrich, D. Nestler, H. Niehoff, P. Wust, B. Thiesen, H. Orawa, V. Budach, A. Jordan, Efficacy and safety of intratumoral thermotherapy using magnetic iron-oxide nanoparticles combined with external beam radiotherapy on patients with recurrent glioblastoma multiforme, J. Neurooncol. 103 (2011) 317–324.
[19] A. Dahaghin, S. Emadiyanrazavi, M. Salimibani, H. Bahreinizad, M. Haghpanahi, R. Eivazzadeh-Keihan, A. Maleki, A numerical investigation into the magnetic nanoparticles hyperthermia cancer treatment injection strategies, Biocybern. Biomed. Eng. 41 (2) (2021) 516–526.
[20] A.A. Golneshan, M. Lahonian, Diffusion of magnetic nanoparticles in a multi-site injection process within a biological tissue during magnetic fluid hyperthermia using lattice Boltzmann method, Mech. Res. Commun. 38 (6) (2011) 425–430.
[21] C. Nicholson, Diffusion and related transport mechanisms in brain tissue, Rep. Progr. Phys. 64 (7) (2001) 815.
[22] M. Roustaei, M. Servatkhah, Effect of mass transfer and diffusion on temperature distribution during magnetic hyperthermia, Phys. B 631 (2022) 413498.
[23] E.H. Ooi, E.T. Ooi, Mass transport in biological tissues: comparisons between single-and dual-porosity models in the context of saline-infused radiofrequency ablation, Appl. Math. Model. 41 (2017) 271–284.
[24] M. Soltani, M.H. Tehrani, F.M. Kashkooli, M. Rezaeian, Effects of magnetic nanoparticle diffusion on microwave ablation treatment: A numerical approach, J. Magn. Magn. Mater. 514 (2020) 167196.
[25] M. Salloum, R. Ma, D. Weeks, L. Zhu, Controlling nanoparticle delivery in magnetic nanoparticle hyperthermia for cancer treatment: experimental study in agarose gel, Int. J. Hyperth. 24 (4) (2008) 337–345.
[26] Y.-d. Tang, T. Jin, R.C. Flesch, Impact of different infusion rates on mass diffusion and treatment temperature field during magnetic hyperthermia, Int. J. Heat Mass Transfer 124 (2018) 639–645.
[27] Y.-d. Tang, T. Jin, R.C. Flesch, Effect of mass transfer and diffusion of nanofluid on the thermal ablation of malignant cells during magnetic hyperthermia, Appl. Math. Model. 83 (2020) 122–135.
[28] K. Erbertseder, J. Reichold, B. Flemisch, P. Jenny, R. Helmig, A coupled discrete/continuum model for describing cancer-therapeutic transport in the lung, PLoS One 7 (3) (2012) e31966.
[29] I. Astefanoaei, I. Dumitru, H. Chiriac, A. Stancu, Thermofluid analysis in magnetic hyperthermia using low curie temperature particles, IEEE Trans. Magn. 52 (7) (2016) 1–5.
[30] M. Zakariapour, M.H. Hamedi, N. Fatouraee, Numerical investigation of magnetic nanoparticles distribution inside a cylindrical porous tumor considering the influences of interstitial fluid flow, Transp. Porous Media 116 (1) (2017) 251–274.
[31] Y. Tang, J. Zou, R.C. Flesch, T. Jin, Backflow modeling in nanofluid infusion and analysis of its effects on heat induced damage during magnetic hyperthermia, Appl. Math. Model. 114 (2023) 583–600.
[32] P. Nithiarasu, K. Seetharamu, T. Sundararajan, Natural convective heat transfer in a fluid saturated variable porosity medium, Int. J. Heat Mass Transfer 40 (16) (1997) 3955–3967.
[33] M. Hamdan, Single-phase flow through porous channels a review of flow models and channel entry conditions, Appl. Math. Comput. 62 (2–3) (1994) 203–222.
[34] X. Chen, P. Yu, S. Winoto, H. Low, Free convection in a porous wavy cavity based on the Darcy-Brinkman-Forchheimer extended model, Numer. Heat Transf. Part A: Appl. 52 (4) (2007) 377–397.
[35] Z. Guo, C. Shu, Lattice Boltzmann Method and its Application in Engineering, Vol. 3, World Scientific, 2013.
[36] J.A. Pedersen, F. Boschetti, M.A. Swartz, Effects of extracellular fiber architecture on cell membrane shear stress in a 3d fibrous matrix, J. Biomech. 40 (7) (2007) 1484–1492.
[37] H. Zhang, Lattice Boltzmann method for solving the bioheat equation, Phys. Med. Biol. 53 (3) (2008) N15.
[38] N.S. Gibanov, M.A. Sheremet, H.F. Oztop, O.K. Nusier, Convective heat transfer of ferrofluid in a lid-driven cavity with a heat-conducting solid backward step under the effect of a variable magnetic field, Numer. Heat Transf. Part A: Appl. 72 (1) (2017) 54–67.
[39] D.D. Gray, A. Giorgini, The validity of the boussinesq approximation for liquids and gases, Int. J. Heat Mass Transfer 19 (5) (1976) 545–551.
[40] Q. Liu, Y.-L. He, Q. Li, W.-Q. Tao, A multiple-relaxation-time lattice Boltzmann model for convection heat transfer in porous media, Int. J. Heat Mass Transfer 73 (2014) 761–775.
[41] B. Wu, J. Lu, H. Lee, C. Shu, M. Wan, An explicit immersed boundary-reconstructed thermal lattice Boltzmann flux solver for thermal–fluid–structure interaction problems, Int. J. Mech. Sci. 235 (2022) 107704.
[42] B. Wu, J. Lu, H. Lee, C. Shu, M. Wan, An explicit boundary condition-enforced immersed boundary-reconstructed thermal lattice Boltzmann flux solver for thermal–fluid–structure interaction problems with heat flux boundary conditions, J. Comput. Phys. 485 (2023) 112106.
[43] W. Yu, H. Xie, A review on nanofluids: preparation, stability mechanisms, and applications, J. Nanomater. 2012 (2012).
[44] P.I. Soares, C.A. Laia, A. Carvalho, L.C. Pereira, J.T. Coutinho, I.M. Ferreira, C.M. Novo, J.P. Borges, Iron oxide nanoparticles stabilized with a bilayer of oleic acid for magnetic hyperthermia and mri applications, Appl. Surf. Sci. 383 (2016) 240–247.
[45] M. Vassallo, D. Martella, G. Barrera, F. Celegato, M. Coisson, R. Ferrero, E.S. Olivetti, A. Troia, H. Sozeri, C. Parmeggiani, et al., Improvement of hyperthermia properties of iron oxide nanoparticles by surface coating, ACS Omega 8 (2) (2023) 2143–2154.
[46] M.W. Dewhirst, B. Viglianti, M. Lora-Michiels, M. Hanson, P. Hoopes, Basic principles of thermal dosimetry and thermal thresholds for tissue damage from hyperthermia, Int. J. Hyperth. 19 (3) (2003) 267–294.
[47] S.A. Sapareto, W.C. Dewey, Thermal dose determination in cancer therapy, Int. J. Radiat. Oncol. Biol. Phys. 10 (6) (1984) 787–800.
[48] S.V. Spirou, M. Basini, A. Lascialfari, C. Sangregorio, C. Innocenti, Magnetic hyperthermia and radiation therapy: radiobiological principles and current practice, Nanomaterials 8 (6) (2018) 401.
[49] S.K. Kandala, E. Liapi, L.L. Whitcomb, A. Attaluri, R. Ivkov, Temperature-controlled power modulation compensates for heterogeneous nanoparticle distributions: a computational optimization analysis for magnetic hyperthermia, Int. J. Hyperth. (2018).
[50] C.L. Carter, C. Allen, D.E. Henson, Relation of tumor size, lymph node status, and survival in 24,740 breast cancer cases, Cancer 63 (1) (1989) 181–187.
[51] A. AlAmiri, K. Khanafer, K. Vafai, Fluid–structure interactions in a tissue during hyperthermia, Numer. Heat Transf. Part A: Appl. 66 (1) (2014) 1–16.
[52] M.A. Swartz, M.E. Fleury, Interstitial flow and its effects in soft tissues, Annu. Rev. Biomed. Eng. 9 (2007) 229–256.
[53] M. Liangruksa, R. Ganguly, I.K. Puri, Parametric investigation of heating due to magnetic fluid hyperthermia in a tumor with blood perfusion, J. Magn. Magn. Mater. 323 (6) (2011) 708–716.
[54] K. Mehmood, S. Hussain, M. Sagheer, Numerical simulation of mhd mixed convection in alumina–water nanofluid filled square porous cavity using kkl model: Effects of non-linear thermal radiation and inclined magnetic field, J. Mol. Liq. 238 (2017) 485–498.
[55] S. Hussain, K. Mehmood, M. Sagheer, M. Yamin, Numerical simulation of double diffusive mixed convective nanofluid flow and entropy generation in a square porous enclosure, Int. J. Heat Mass Transfer 122 (2018) 1283–1297.
[56] Z. Guo, T. Zhao, Lattice Boltzmann model for incompressible flows through porous media, Phys. Rev. E 66 (3) (2002) 036304.
[57] Q. Liu, Y.-L. He, Multiple-relaxation-time lattice Boltzmann model for simulating double-diffusive convection in fluid-saturated porous media, Int. J. Heat Mass Transfer 127 (2018) 497–502.
[58] J. Lang, B. Erdmann, M. Seebass, Impact of nonlinear heat transfer on temperature control in regional hyperthermia, IEEE Trans. Biomed. Eng. 46 (9) (1999) 1129–1138.
[59] J. Buongiorno, Convective transport in nanofluids, J. Heat Transf. (2006).
[60] E. Tzirtzilakis, A mathematical model for blood flow in magnetic field, Phys. Fluids 17 (7) (2005) 077103.
[61] S. Purushotham, R. Ramanujan, Modeling the performance of magnetic nanoparticles in multimodal cancer therapy, J. Appl. Phys. 107 (11) (2010) 114701.
[62] L. Roizin-Towle, J.P. Pirro, The response of human and rodent cells to hyperthermia, Int. J. Radiat. Oncol. Biol. Phys. 20 (4) (1991) 751–756.
[63] Q. Jiang, F. Ren, C. Wang, Z. Wang, G. Kefayati, S. Kenjeres, K. Vafai, Y. Liu, H. Tang, On the magnetic nanoparticle injection strategy for hyperthermia treatment, Int. J. Mech. Sci. 235 (2022) 107707.
[64] L.T. Baxter, R.K. Jain, Transport of fluid and macromolecules in tumors. I. Role of interstitial pressure and convection, Microvasc. Res. 37 (1) (1989) 77–104.
[65] I. Raouf, J. Lee, H.S. Kim, M.-H. Kim, Parametric investigations of magnetic nanoparticles hyperthermia in ferrofluid using finite element analysis, Int. J. Therm. Sci. 159 (2021) 106604.
[66] S. Dutz, R. Hergt, Magnetic nanoparticle heating and heat transfer on a microscale: Basic principles, realities and physical limitations of hyperthermia for tumour therapy, Int. J. Hyperth. 29 (8) (2013) 790–800.
[67] A. Hervault, N.T.K. Thanh, Magnetic nanoparticle-based therapeutic agents for thermo-chemotherapy treatment of cancer, Nanoscale 6 (20) (2014) 11553–11573.
[68] S. Mondal, P. Sibanda, Effects of buoyancy ratio on unsteady double-diffusive natural convection in a cavity filled with porous medium with non-uniform boundary conditions, Int. J. Heat Mass Transfer 85 (2015) 401–413.
[69] G.R. Kefayati, H. Tang, Double-diffusive natural convection and entropy generation of carreau fluid in a heated enclosure with an inner circular cold cylinder (part i: Heat and mass transfer), Int. J. Heat Mass Transfer 120 (2018) 731–750.
[70] T. Vijaybabu, Influence of porous circular cylinder on mhd double-diffusive natural convection and entropy generation, Int. J. Mech. Sci. 206 (2021) 106625.
[71] K.H. Bae, M. Park, M.J. Do, N. Lee, J.H. Ryu, G.W. Kim, C. Kim, T.G. Park, T. Hyeon, Chitosan oligosaccharide-stabilized ferrimagnetic iron oxide nanocubes for magnetically modulated cancer hyperthermia, ACS Nano 6 (6) (2012) 5266–5273.
[72] Z. Hedayatnasab, F. Abnisa, W.M.A.W. Daud, Review on magnetic nanoparticles for magnetic nanofluid hyperthermia application, Mater. Des. 123 (2017) 174–196.
[73] R.W. Habash, R. Bansal, D. Krewski, H.T. Alhafid, Thermal therapy, part 1: an introduction to thermal therapy, Crit. Rev.™ Biomed. Eng. 34 (6) (2006).

[74] Z. Wang, C. Wang, F. Zhao, N. Qi, D. Lockington, K. Ramaesh, P.S. Stewart, X. Luo, H. Tang, Simulation of fluid–structure interaction during the phaco-emulsification stage of cataract surgery, Int. J. Mech. Sci. 214 (2022) 106931.

[75] F. Ren, C. Wang, H. Tang, Active control of vortex-induced vibration of a circular cylinder using machine learning, Phys. Fluids 31 (2019) 093601.

[76] C. Wang, H. Tang, F. Duan, C. Simon, Control of wakes and vortex-induced vibrations of a single circular cylinder using synthetic jets, J. Fluids Struct. 60 (2016) 160–179.

[77] K. Das, S.C. Mishra, Estimation of tumor characteristics in a breast tissue with known skin surface temperature, J. Therm. Biol. 38 (6) (2013) 311–317.

[78] K. Das, R. Singh, S.C. Mishra, Numerical analysis for determination of the presence of a tumor and estimation of its size and location in a tissue, J. Therm. Biol. 38 (1) (2013) 32–40.

[79] P. Lallemand, L.-S. Luo, Theory of the lattice Boltzmann method: Dispersion, dissipation, isotropy, galilean invariance, and stability, Phys. Rev. E 61 (6) (2000) 6546.

[80] B. Ghasemi, S. Aminossadati, A. Raisi, Magnetic field effect on natural convection in a nanofluid-filled square enclosure, Int. J. Therm. Sci. 50 (9) (2011) 1748–1756.